UNIVERSITY OF KWAZULU-NATAL ™

INYUVESI YAKWAZULU-NATALI

Study on extreme geomagnetic events and ionospheric response

by

Adila Wamisho Tire

A thesis submitted as the dissertation component in partial fulfillment of the academic requirement for the degree of Master of Science in the school of Chemistry and Physics, University of KwaZulu-Natal.

May 2018

Study on extreme geomagnetic events and ionospheric response

by
Adila Wamisho Tire

A thesis submitted as the dissertation component in partial fulfillment of the academic requirement for the degree of Master of Science in the school of Chemistry and Physics, University of KwaZulu-Natal.

As the candidate's supervisor, I have approved this thesis for submission.

Supervisor Signed:_____ Name:_____

Date:_____

Co-Supervisor Signed:_____ Name:_____

Date:_____

Abstract

Extreme geomagnetic events are geophysical phenomena that result from the violent eruptive nature of the Sun. One type Geospace event is magnetic cloud (MC), which is an attendant of coronal mass ejection (CME). MC-triggered storms can cause injection of particles into the ionosphere. This can result in an enhance ionization and conductivity of upper and middle atmosphere. MC can be identified based on geomagnetic parameters and solar wind conditions which show high magnetic field magnitudes, low ratio of plasma to magnetic pressure, low proton temperature, and smooth rotation of the magnetic field vector. MC events that occurred on 29 April 2014, 17 March 2015, 31 December 2015 and 13 October 2016 were selected for the study. The hourly average of particle dropouts, precipitation, local ionospheric response and magnetometer variations in the region over South Africa (33.3^{o}S, 26.5^{o}E) are examined during geomagnetic storms triggered by MC. The Geostationary Operational Environmental Satellites (GOES) were inspected for radiation belt particle dropouts during MC events. Energetic particle precipitation associated with MC events are obtained from National Oceanic and Atmospheric Administration (NOAA) Polar Orbiting Environmental Satellites (POES). Results show that particle dropouts and precipitation vary with the arrival of MC. A closer look of the ground based magnetometer and the time history of available daytime E-layer critical frequency from ionosonde indicate that lower ionosphere respond to MC-driven storm.

Preface

The work contained in this thesis was carried out from April 2016 to May 2018 in the School of Chemistry and Physics, University of KwaZulu-Natal, Westville campus, South Africa, under the Supervision of Professor Sivakumar Venkataraman and Co-Supervision of Doctor Olakunle Ogunjobi.

Student Signed:_____ Name:_____

Date:_____

Declaration - Plagiarism

I, Adila Wamisho Tire declare that

i. This work has been composed solely by myself, except where stated otherwise by reference or acknowledgement, the work presented is entirely my own.

ii. This work has not been submitted, in whole or in part, in any previous application for a degree.

Signed: _____

The *field* is perturbed!

Acknowledgements

I would like to express my sincere gratitude to my supervisors, Professor Sivakumar Venkataraman who took me as his student under National Astrophysics and Space Science Programme (NASSP) and Dr Olakunle Ogunjobi for his co-supervision. Their expert guidance, support and patience made my struggle easy throughout this work. I would like to extend my appreciation to South African National Space Agency (SANSA) for providing me local Ionosonde data which I needed for this study. I am grateful to Mr. Bernard Mmame for his friendship support and all my friends for their encouragement. My final thanks goes to my family who always believe in me even in my worst times.

Contents

List of Figures

List of Tables

Abbreviations

AU	Astronomical Unit
CME	Coronal Mass Ejection
EPP	Energetic Particle Precipitation
EPEAD	Energetic Proton, Electron and Alpha Detector
EUV	Extreme Ultraviolet
GOES	Geostationary Operational Environmental Satellites
GSM	Geocentric Solar Magnetospheric
GSO	Geosynchronous Orbit/ Geostationary Orbit
HF	High Frequency
IGRF	International Geomagnetic Reference Field
ICME	Interplanetary Coronal Mass Ejection
IMF	Interplanetary Magnetic Field
LEO	Lower Earth Orbit
MC	Magnetic Cloud
MLT	Mesosphere and Lower Thermosphere
NASA	National Aeronautic and Space Administration
NOAA	National Oceanic and Atmospheric Administration
NSSDC	National Space Science Data Center
POES	Polar Orbiting Environmental Satellites
QBO	QuasiBiennial Oscillation
SANSA	South African National Space Agency
SPE	Solar Proton Event
VLF	Very Low Frequency

Chapter 1

Introduction

This study examines the response of South African ionospheric region during Geospace event. A synthesis of multiple observations is performed to investigate the response of the outer radiations belt and mid-latitude ionosphere to energetic particle dropouts and precipitation, respectively. This is done in order to have a complete sequential overview of the magnetospheric-ionospheric relationships during extreme Geospace events. The magnetosphere-ionosphere need to be considered simultaneously if we desire a consistent and complete overview of the effects of particle precipitation at the middle atmosphere in particular during Geospace events. During such events, the middle atmosphere can experience increase in ionisation and excitation from particle precipitation.

This is possible because Geospace event can cause energetic particle to get loss from trapped radiation belt, which is embedded in the magnetosphere, and consequently precipitate into the atmosphere. Although the sources of the precipitating particles are many and varied. However, the most important sources involve coupling Sun-Earth connection phenomena. One of such important source is the Van Allen radiation belts. The Van Allen radiation belts are regions of trapped high-energy particles, primarily electrons and protons, which are trapped by the magnetic influence of the Earth. It is generally known that the effect of energetic particle precipitation from the radiation belt is more pronounced in the high-latitude polar regions. However, the possibility of aurora in the mid-latitude and the attendant particle precipitation have been a great concern and still an exigent scientific discussion. In this present work, the possible occurrence of precipitation triggered by extreme Geospace event over the South African ionosphere, a mid-latitude region, is examined. Since South Africa is at the vicinity of South Atlantic Anomaly, precipitation effect over

this region is possible. One type of Geospace event that could cause trapped particles to dropout of radiation belts and ultimately influence particle precipitation is known as magnetic cloud (MC) event. In this study, the MC events that occurred on 29 April 2014, 17 March 2015, on 31 December 2015 and on 13 October 2016 were characterized and the associated dropouts and precipitation were investigated.

More precisely, precipitation involves the inflow of energy from the radiation belt, embedded in the Earth's magnetosphere, into the ionosphere. Energetic particle precipitation is a form of space-weather phenomenon, which can have serious effects on space-based and ground-based technological systems. Its effects on ionospheric variation cannot be overemphasised. Such effects ranges from radio communication and navigation problems to satellite solid state surges. Furthermore, any ionospheric changes caused by space weather effect can result in propagation signal loss posing security challenges. So, the importance is not only significant for scientist that try to understand the principal mechanism causing precipitation, but also military and civilian usage of various technological systems. For instance, ionospheric scintillation, resulting from the space weather effect, can cause Global Positioning Systems (GPS) error.

In this project we have used both ground based ionospheric monitoring data and satellite data to study the MC triggered storm. This thesis presents an account of our investigation into the effects that MC event has on the South African ionospheric region. Chapter two presents a detailed theoretical background to energetic dropouts, precipitation and the relevant source of these particles as well as mode of their interaction with the Earth's magnetosphere and ionosphere. Chapter three presents satellite and ground based data we have employed for this study as well event selection and characterization. Chapter four presents the analysis trapped energetic particles, using space based instruments. Ionospheric response analyzed using ground based ionosonde and magnetometer data is discussed and presented in chapter five. At the end, chapter six presents the summary and some possible future works which can be extended from the results.

Chapter 2

Theory and background of the study

This chapter presents solar terrestrial connection and also reviews past works on the responses of the middle atmosphere to geomagnetic storm. The review includes the coronal mass ejection (CME) in relation to magnetic cloud that leads to energetic particle dropouts. We also provided the basic of the effect that precipitation could have on near Geospace environment particularly magnetosphere-ionosphere.

2.1 The Sun and solar wind

The Sun is an ordinary magnetic star of intermediate size and temperature, as astrophysicist describe it (May-Britt, 2001). There is no other star in the Universe which is so close to the Earth and has such great influence on our day to day lives and the Earth's atmosphere in general, as a result the Sun is the most interesting star. Its proximity allows us to study its electromagnetic radiation and energetic particles emissions and their effect like no other star in the Universe. The study of Sun also enlightened the understanding of other far stars which only their electromagnetic (optical) radiation are accessible for scientific studies. The Sun constitutes of hydrogen (about 90%) as the fuel of solar energy, helium (about 10%) and very small fraction of other heavier elements (Priest ((1995)) and May-Britt, 2001). The elements in the Sun are highly ionized due to extremely high temperature ($\backsim 1.5 \times 10^7 K$) as a result of nuclear fusion reaction at the core which made Sun the source of energy for our solar system.

The high temperature assists electrons to escape from the binding energy of atoms. The excess unbounded charged particles create a huge electromagnetic field which can accelerate the charged particles outwards. Also enormous plasma pressure difference created between solar corona and interstellar space drive the solar plasma outward allowing solar participles to escape the strong solar gravity as showen in Figure: 2.1.

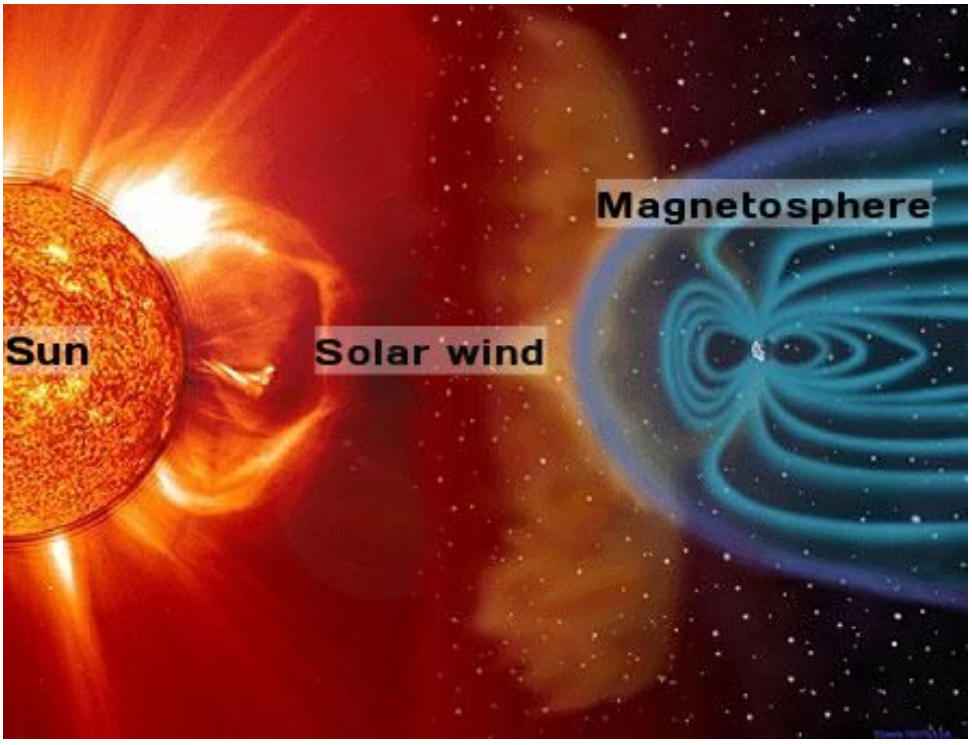

Figure 2.1: An artistic picture showing how the solar wind originate from the Sun and impact the magnetosphere. Adapted from https://sohowww.nascom.nasa.gov/gallery/images/magfield.html. Accessed on 5 April 2017.

The continuous streaming solar particles appear to have high speed (300 - 800 km/s) with typical density of 6.6 cm^3 for protons and 7.1 cm^3 for electrons. The flow of ionized solar plasma that interpenetrates interplanetary space referred to as solar wind. The theory of particle flow from the Sun in interplanetary space was suggested at the beginning of the twentieth century and the direct observation was started in 1960 (May-Britt, 2001). There are fast solar wind and slow solar wind identified from observation. The fast solar wind originates from coronal holes which is the dark part of the corona in which open magnetic field lines are dominant. On the other hand the slow solar wind originates from regions close to the currents sheet at the solar equator during solar minimum and above active regions in streamer belt during solar maximum. Typical values for the solar wind plasma and magnetic field near the Earth are given in Table 2.1.

Table 2.1: Observed properties of the solar wind and magnetic field near the orbit of Earth (1 AU) as presented by Kivelson and Russell, 1995.

Parameter	Observed Value
Proton density	6.6 $cm^{-}3$
Electron density	7.1 cm^{-3}
He^{2+} density	0.25 cm^{-3}
Flow speed (nearly radial)	450 $km.s^{-1}$
Proton temperature	1.2×10^{5} K
Electron temperature	1.4×10^{5} K
Magnetic field	5.0×10^{-9}tesla(T)

2.1.1 Coronal mass ejections

Coronal mass ejections (CMEs), first observed with advanced space-craft coronographs in 1980, are occasional violent manifestations of solar activity (Dungey, 1961 and Kivelson and Russell, 1995). During CME a huge mass (approximately a billion tons) of solar material and energy, stored in the magnetic field blast radially away with a speed of over 1000 km/s, from the Sun to the interplanetary space (Kivelson and Russell, 1995). The number of CMEs depend on solar cycle properties such as magnetic field, sunspots, and filaments. A great number of CMEs are observed during solar maximum compared to solar minimum. CMEs are distributed evenly on both sides of the hemispheres and the impact of the Earth depends on where they originated on the Sun and geo-location of the Earth. CMEs originated relatively near to the Sun equator and directed to the Earth will have the most likely a direct hit on the Earth. These direct hits can cause major geomagnetic storms when it interacts with the Earth's magnetic field and therefore CMEs are one of the most important space weather phenomena. Figure 2.2 presents a large coronal mass ejection ejects a cloud of particles into space as seen by cononagraph.

2.1.2 The interplanetary magnetic field

The Sun has complex internal magnetic field which arises from its plasma dynamics. The magnetic field, called interplanetary magnetic field (IMF), is frozen into highly conductive solar wind and carried out into interplanetary space (Dungey, 1961 and Kivelson and Russell, 1995). Due to the rotation of the Sun, the solar wind that flows radially away from the Sun, carrying the frozen-in magnetic field, have a spiral structure (Jursa et al., 1985). However, the complex nature and varying magnetic field of the Sun continuously modifies the spiral structure of the IMF to form Archimedean (arithmetic) spiral or logarithmic spiral. In addition to the spiral pattern, the IMF has north-south (up-dawn) wavy pattern confirmed from heliospheric current sheet.

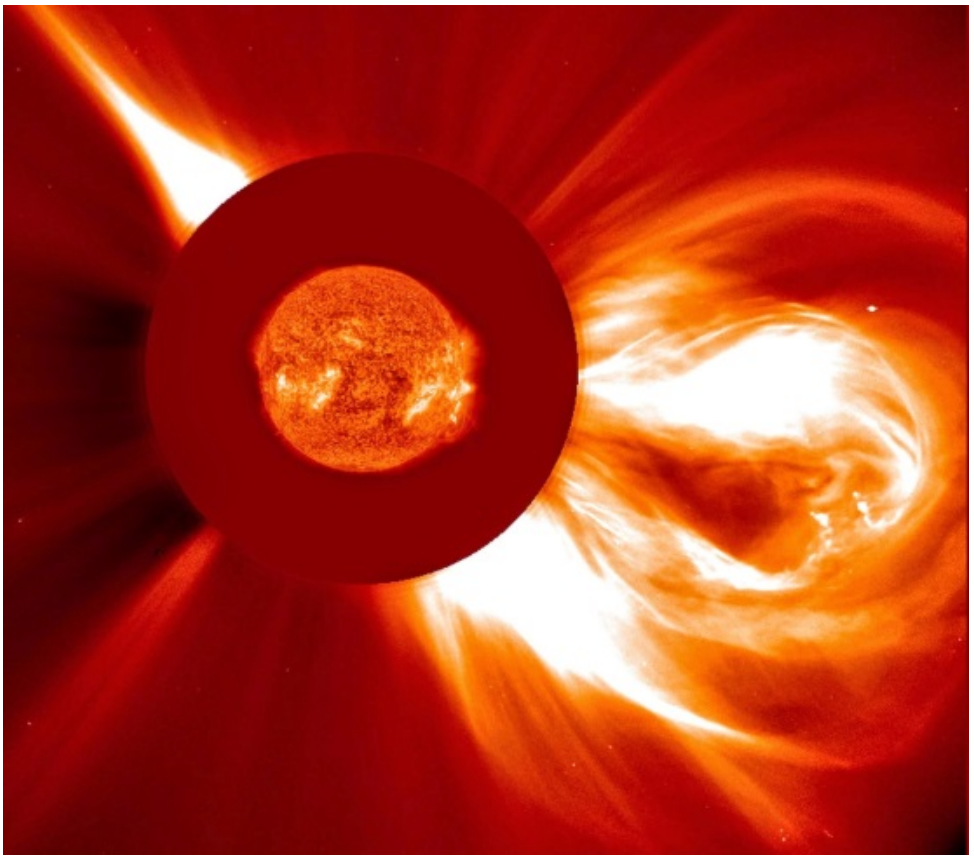

Figure 2.2: A coronal mass ejection erupting at the Sun as observed by coronagraph on 2 December 2003. Obtained from https://sohowww.nascom.nasa.gov/gallery/images/20031202c2eit304.html. Accessed on 10 April 2017.

The Sun have solar cycle which can be observed from patterns of solar activities change. The solar cycle which is strongly linked to sunspots number (one of solar activities) greatly affects photospheric magnetic field, subsequently vary the IMF. The population of sunspots which vary in about 11-year period are strong indicators of solar cycle. Typical magnitudes of the IMF at 1 AU are $\simeq$ 5 nT (Table 2.1) and during high solar activity the strength of the IMF enhance more than 25 nT.

2.2 Earth's magnetic field and the magnetosphere

The Earth has intrinsic magnetic field resulted from the dynamo motion within the Earth itself. In a normal condition at the vicinity of the Earth surface the magnetic field can be approximated as dipole (with dipole moment $M_E = 8 \times 10^{25}$ G.cm^3). However, activities which are driven by the conditions of the Sun such as solar wind pressure, plasma current and field exchange with the interplanetary space medium

significantly modify the dipole configuration (Kivelson and Russell, 1995). The respective geomagnetic poles of the Earth tilted by about 11.3° from the geographic poles with respect to the axis of rotation. The geomagnetic longitude Λ and latitude Φ are related to geographic longitude λ and latitude φ by transformation equations given as,

$$\sin\Phi = \sin\varphi \sin\varphi_o + \cos\varphi \cos\varphi_o \cos(\lambda - \lambda_o) \tag{2.1}$$

and,

$$\sin\Lambda = \frac{\cos\varphi \sin(\lambda-\lambda_o)}{\cos\Phi} \tag{2.2}$$

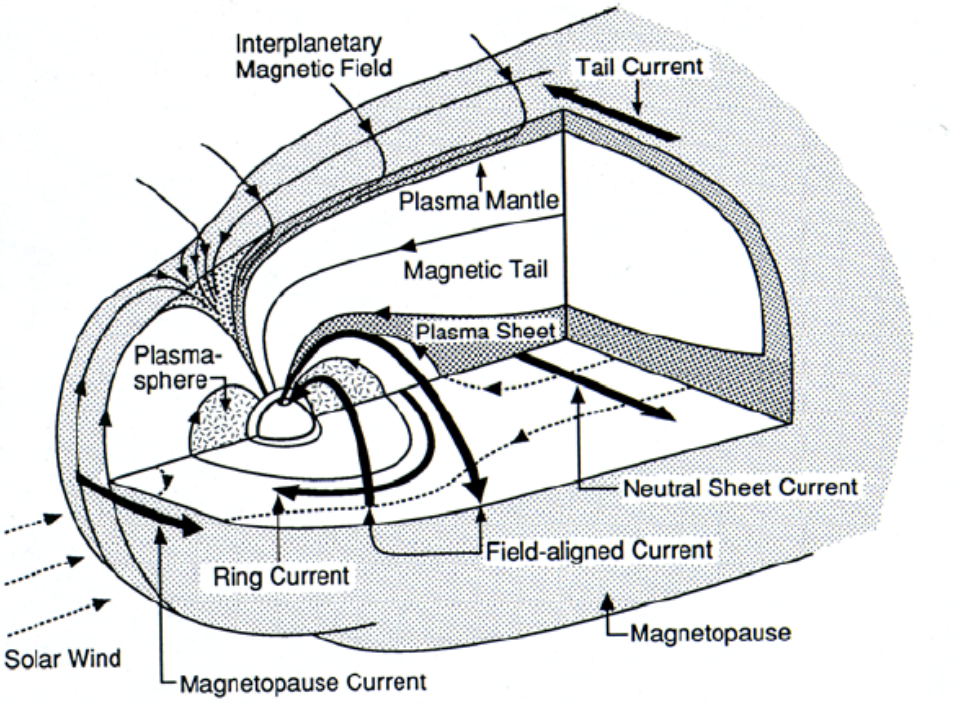

Figure 2.3: Cutaway drawing of magnetosphere showing the IMF, magenetopuse and different plasma current systems. Obtained from Kivelson and Russell, 1995.

The field lines are approximated using the L-value parameter which is a dipole magnetic field line coordinate given as, (McIlwain, 1966 and Merrill and McElhinny, 1983).

$$\Lambda = \cos^{-1}(\frac{1}{L})^{1/2} \tag{2.3}$$

The L-value is a distance with the magnitude of Earth radius (R_E) from the center of the Earth to the magnetic field line along equator, for example, a field line which is at a distance 3 R_E from the center of the Earth along the equator will have $L \backsim 3$. This L-value is found to be related to the magnetic latitude(Λ) as given by equation (2.3). L-value is perhaps a true estimation of complex magnetic field of the Earth (Varotsou

et al., 2008), however the IMF and solar wind effects on the Earth's magnetic field magnify by adding complexity and result inaccurate values at lower L.

The magnetosphere is near-Earth space plasma cavity of solar wind that enclose the Earth's magnetic field. It is created when solar wind interact with the magnetic field of the Earth (see Figures 2.1 and 2.3). The boundaries of the magnetosphere are controlled by the balance of the streaming solar wind dynamic pressure and magnetic pressure of Earth's dipole field (Kivelson and Russell, 1995 and May-Britt, 2001). The estimation of this balance is expressed in equation (2.4)

$$p_{mag} = \frac{B_t^2}{2\mu_o} \tag{2.4}$$

where p_{mag} is the magnetic pressure, B_t is the tangential magnetic field and μ_o is constant. The magnetic pressure is not constant over the boundary surface, hence this requires the solar wind velocity to vary to balance the magnetic pressure.

The clear boundary separating the magnetosphere from the solar wind is called the magnetopause (see Figure: 2.3), which is created at the pressure balance stand-off. The day and the night sides of these boundaries have different shape and size. On the day-side, the magnetosphere has spherical type of shape and extends about 9 to 11 Earth radii (R_E = 6378 km) whereas on the night-side magnetosphere deformed into a comet-tail shape and extend well beyond 60 R_E (Roelof and Sibeck, 1993) (see Figure 2.3). Upon the impact of geomagnetic storms, the magnetosphere is compressed towards the Earth on the day-side and the size decreases significantly. The magnetosphere has plasma of solar origin mainly protons and electrons, as well as heavier ions. Depending on these plasma density, magnetic field and temperature, the magnetosphere is subdivided into different regions such as the plasmasphere, the Van Allen radiation belt, the plasmasheet and the magnetotaile lobe, as annotated in Figure 2.3.

2.2.1 Radiation belts

The discovery of radiation belts in 1958 was accidental but significant scientific result of space research with satellites by group led by Van Allen (Van Allen and Frank, 1959). They noticed that the Geiger counter which was meant for cosmic ray detection on board the spacecraft measured unexpected too low or too large signatures of radiations. But from the pattern of observations it has become evident that unexpected signals always indicate particle fluxes much higher than expected. This confirmed the existence of the radiation belts which extend from a few hundred km

above the Earth to about 7 R_E. Figure (2.4) shows the radiation belts and some LEO, GSO and van Alen Probe satellites.

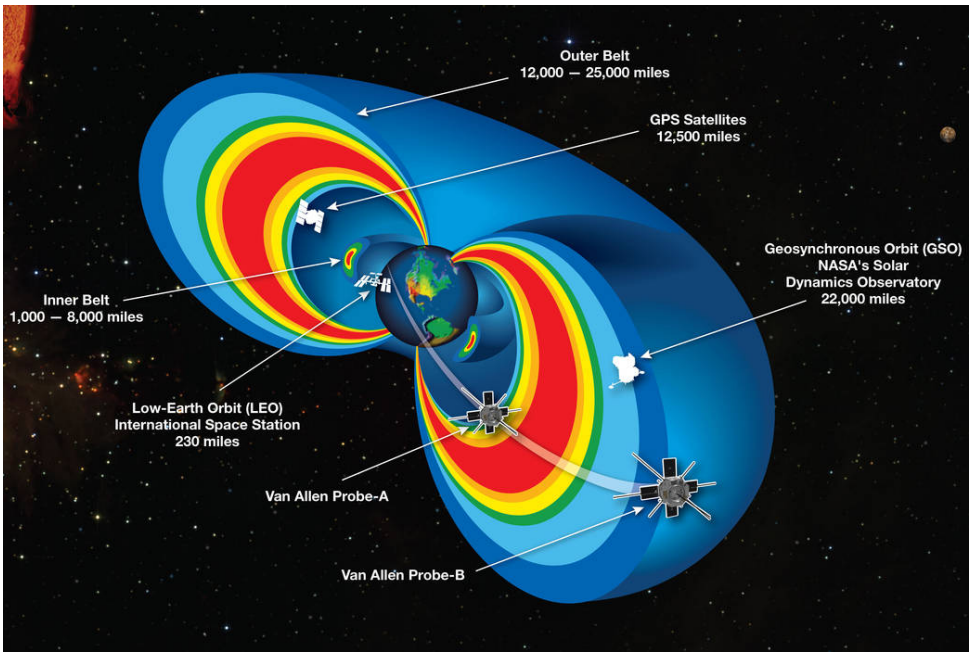

Figure 2.4: A cutaway model of radiation belts. Obtained from https://www.nasa.gov/missionpages/sunearth/news/gallery/20130228radiationbelts.html Accessed on 25 April 2017.

When solar wind impacts the magnetosphere some of the energy and charged particles are trapped in the magnetic field and when they are released they crates enormous acceleration of particles which has hazardous impact. The radiation belt effective hinders most of the charged particles from entering the Earth atmosphere. The radiation belt is often divided into two zones (Figure 2.4), the inner with L $<$ 2 and the outer with L $>$ 2. The inner zone particle populations are small stable and long-lived compared to particle populations in the outer zone which depend on solar wind conditions and geomagnetic activity. The evolution of the inner belt is due to the influence of losses because of Coulomb scattering (Thorne, 2010) while the outer radiation belt with highly dynamic electron populations. Recent radiation belt probe spacecraft observations showed that there is an isolated unstable belt within about 3 to 3.5 L-value which comprise of electrons with energy of 2 MeV (Baker et al., 2013).

The particles in the radiation belt, as charged particles in a magnetic field, undergo gyration, bounce, and drift motions as shown in Figure: 2.5. The gyration around magnetic field lines is due to perpendicular component of the velocity to the magnetic field lines, the bounce motion along field lines between magnetic mirror points is due to the parallel of velocity component to the field lines, and the drift motion around the Earth is due to magnetic gradient and curvature drifts.

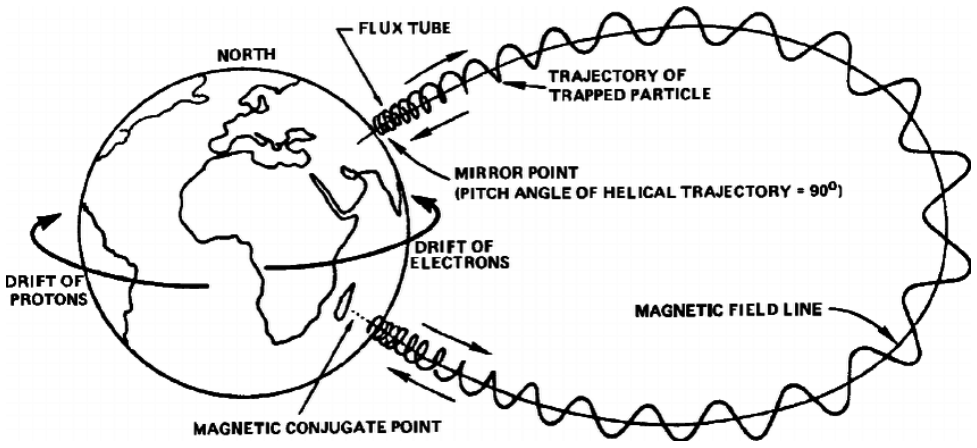

Figure 2.5: Schematic diagram of charged particles motion in radiation belts. Obtained from Jursa et al., 1985.

The motions are described by the adiabatic invariant (Chen and von Goeler, 1985). However during geomagnetic storms magnetic fluctuations and magnetospheric disturbance alter the stability. If electric field $\mathbf{E}$ and a magnetic induction $\mathbf{B}$ act on a charged particle q which is moving with a velocity $\mathbf{v}$, the particle experiences a force called Lorentz force, it is given by the equation (2.5)

$$\mathbf{F} = q(\mathbf{E} + \mathbf{v} \times \mathbf{B}) \tag{2.5}$$

The charged particle gyrates around the magnetic field lines with a normal component of the velocity ($v_\perp$). The spiral diction of gyral motion of electrons and protons are in opposite due to their charges. The gradient force control the bounce motion and given by equation (2.6)

$$\mathbf{F} = (\mu \bigtriangledown)\mathbf{B} \tag{2.6}$$

where μ is magnetic moment and if m is the mass of the particle, the magnetic moment which is the first adiabatic invariant expressed as,

$$\mu = \frac{mv_\perp^2}{2B} \tag{2.7}$$

The particle moves in such a way that increasing its perpendicular velocity at cost of decreasing its parallel velocity to the pole where the field lines close to each other. The gradient force bounces the particles at the mirror point along the field lines back to the opposite pole (Figure 2.5). This bounce motion is almost periodic between the two mirror points and the constant of the motion, the longitudinal invariant J, become the second adiabatic invariant and between any two points a and b given by

$$J = \int_a^b v_\parallel ds \tag{2.8}$$

The drift of a guiding center around the Earth (Figure 2.5) constitutes the drift motion. This drift motion is linked to the third adiabatic invariant, total magnetic flux Φ which is enclosed by the drift surface. The period of the drift motion is relatively long but magnetic field variation occur on a shorter time scale as a result the third adiabatic invariant has only few applications.

2.3 The ionosphere

The ionosphere is part of the Earth's atmosphere approximately above 50 km from the ground which is characterized by ionized gas (Ratcliffe, 1972 and Kelley, 2009). The solar ultraviolet radiation and energetic participles precipitating from the Sun and the radiation belt to the atmosphere excite and ionize the neutral atmosphere. Based on ionized gases density, ionosphere is generally subdivided into D-region (60 to 90 km), E-region (90 to 150 km) and F-region (150 km and above) layers. The plasma density in the D-region is about 500 cm^{-3} which mostly ionized by the UV radiation and X-rays enhance ionization rates during solar flares. This region absorbs short wave radio frequencies and affected by the dynamics of neutral atmosphere (due to its proximity to the neutral atmosphere). The plasma density in the E-region reaches to 10^5 cm^{-3}, as a result this region is highly conductive compared to D-region. The F-region is known for its very high plasma density, 10^6 cm^{-3}. Unlike D and E regions, the F-region has less day/night times variation. Figure 2.6 presents typical temperature and electron density profiles of the atmosphere.

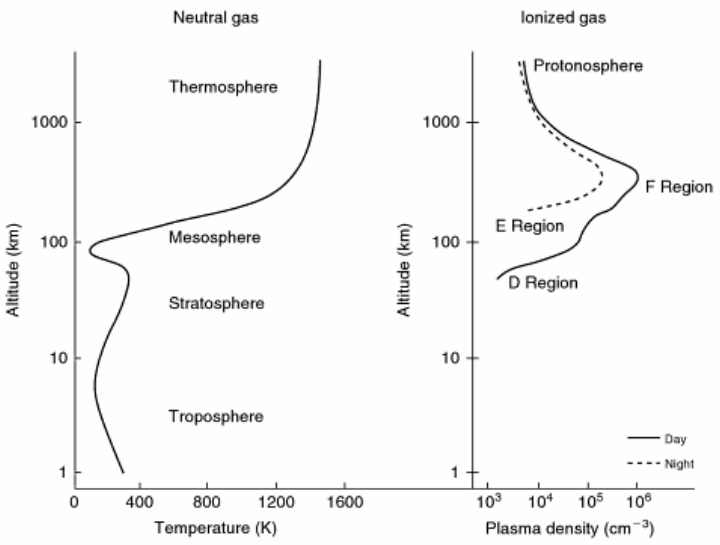

Figure 2.6: Typical temperature and plasma density profile of the atmosphere. Obtained from Kelley, (2009).

The middle atmosphere, mesosphere (60 to 100 km) and lower thermosphere (100 to 180 km) are parts of the lower ionosphere. The mesosphere and lower thermosphere regions (MLT) are less understood considering the energy budget because of the complex interaction in the region.

2.4 Geomagnetic storms

As discussed in the above sections, the Sun continuously blows solar wind, magnetized charged particles and energy, into the interplanetary space in all directions. When the solar wind impacts the Earth magnetosphere, some of the solar wind particles and energy are trapped in Earth's magnetic field. The magnetosphere is in a continuous stress because of energy released to it which produces enormous acceleration of particles that account for radiation belt and aurora. On top of that, the Sun occasionally blast coronal mass ejections (CMEs) and those CMEs are directed to Earth which hit already stressed Earth's magnetic field resulting to a magnetic disturbance called geomagnetic storm (Gonzalez et al., 1994 and Bothmer and Daglis, 2007). The geomagnetic activity increases energetic particles in the ring current which produces an induced magnetic field.

The severity of the disturbance measured using the index called storm-time disturbance index (D_{st}) (Gonzalez et al., 1994 and Campbell, 1996). The D_{st} index, which is measured in nanoteslas (nT), is a useful observation to identify and classify geomagnetic disturbances. In general, geomagnetic storm has three phases. The disturbance starts with a small enhancement of D_{st} due to magnetosphere Earthward compression which is resulted by solar wind pressure, sudden storm commencement. This result to a sudden increase in the ring current (intensification of ring current) which leads to a rapid decrease of D_{st}, the main phase, followed by a prolonged recovery phase. The geomagnetic storms loosen the safeguard of trapped energetic particles allowing them to precipitate into the atmosphere. When energetic particles access the high altitude atmosphere through ionization, they change the composition and energy of MLT (Thorne, 1980 and Ogunjobi et al., 2014).

2.4.1 Geomagnetic storm index

The geomagnetic variation can be measured by standard magnetograms. The magnetograms and the averaged data obtained from the magnetic observatories have since been found extremely useful to compute some numerical parameters that indicate the level of general magnetic disturbance. Storms are measured by the K-index which

is the overall geomagnetic condition of the upper atmosphere over the past 3 hours and ranges quasi-logarithmically from 0 to 9. Although some interfaces can refer to it in multiple of 10. The K_p index (p for planetary) is a measure of magnetospheric activity which indicates the strength of solar wind driving the magnetosphere. K_p index has a similar usage as the hourly D_{st} index for mid to low-latitude activity. It is the magnitude of the normalized horizontal component of the equatorial magnetic field and routinely obtained by mid-latitude observatories network of ground-based magnetometers located around the globe. The D_{st} index was designed as a measure of magnetospheric ring current (see Figure 2.3). Most of the activity indices increase with the square of solar wind velocity. Nevertheless, almost no magnetic activity is seen unless the IMF embedded in the solar wind has a southward component, antiparallel to the Earth's magnetic field near the subsolar point on the dayside magnetopause.

2.4.2 Magnetic clouds

The observation of coronal mass ejections (CMEs) started in 1980 with coronograph (see Figure 2.2) using space borne measurements (Hundhausen, 1999). CMEs are the most eruptive manifestations of solar activity and a high speed attended by coronal materials escape the gravitational attraction of the Sun (Kahler, 1987). Morrison (1954) postulated that the material ejected from the Sun carry solar magnetic field which he called them magnetic clouds (Parker, 1965). Magnetic clouds, (see Figure 2.7), are directly linked to CMEs (Burlaga, 1991 and Richardson and Cane, 2010), however not all CMEs result MCs because some CMEs carry disordered non-geoeffective magnetic field (Burlaga et al., 2002).

Goldsteion (1983) proposed a model of force-free magnetic field configuration to represent magnetic clouds. A force-free magnetic field can be solved from,

$$\mu_o \mathbf{j} = \nabla \times \mathbf{B} = \alpha \mathbf{B} \tag{2.9}$$

If α is constant, equation (2.9) reduces to,

$$\nabla^2 B + \alpha^2 B = 0 \tag{2.10}$$

Burlaga (1998) showed that the constant α of the force-fee magnetic field determines the magnetic field variations when MC sweep a spacecraft. The solutions of equation

(2.10), using cylindrical symmetry as given by Lundquist (1986), are

$$\begin{aligned} B_R &= 0 \\ B_\Phi &= HB_o J_1(\alpha R) \\ B_Z &= B_o J_o(\alpha R) \end{aligned} \tag{2.11}$$

where R, Φ and Z are respective cylindrical coordinates, J_o and J_1 are Bessel functions and $H = \pm 1$ indicates the chirality of the magnetic field. Other magnetic cloud models include toroidal loop model (Chen and Garren, 1993) and non-force-free model (Hidalgo et al., 2002).

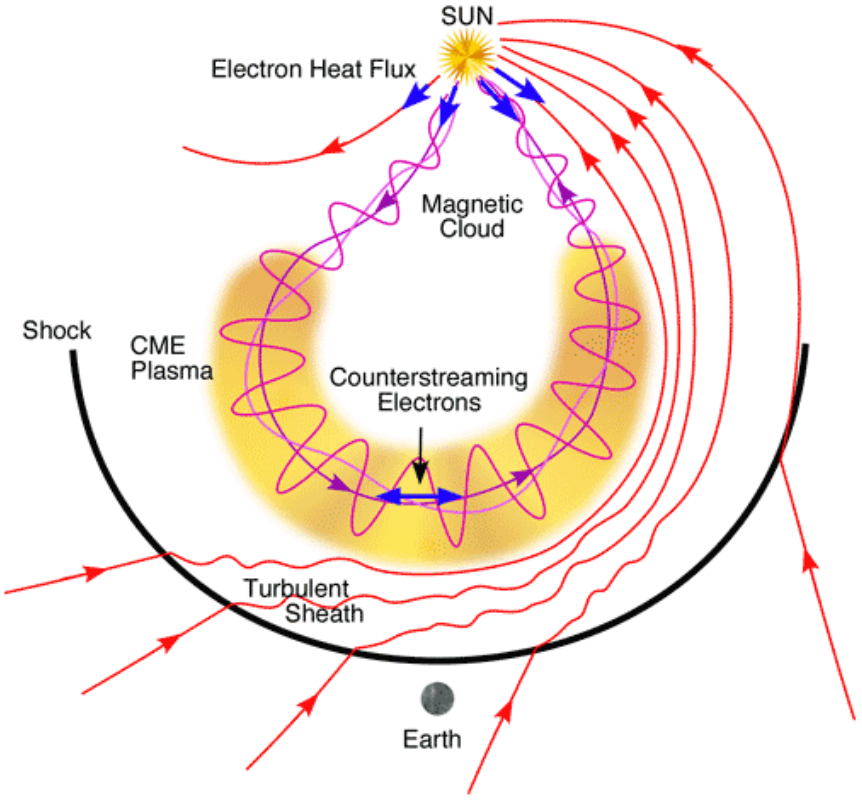

Figure 2.7: Schematic diagram of magnetic cloud after eruption of CME. Obtained from Zurbuchen and Richardson, 2006.

MCs are important space weather features because of the magnetic storm they impose. From observation, MCs are characterized by enhanced total magnetic field, low ratio of plasma to magnetic pressure (plasma beta), low ion temperature and smooth rotation of the magnetic field vector through a large angle (Burlaga et al., 1981). Tsurutani and Gonzalez (1995) suggested that the MCs most likely correspond to relatively dark region of the CME. This is because one of the properties of MC is low ion temperatures (Farrugia et al., 1997). Lepping (1997) further noted that MCs are identified in the boundary that the leading half of the southward turning of the z-component of the magnetic field vector followed by the strong northward

turning otherwise the interchange of southward northward turning of the magnetic field vector. The important properties of MC are presented in Figure 2.8.

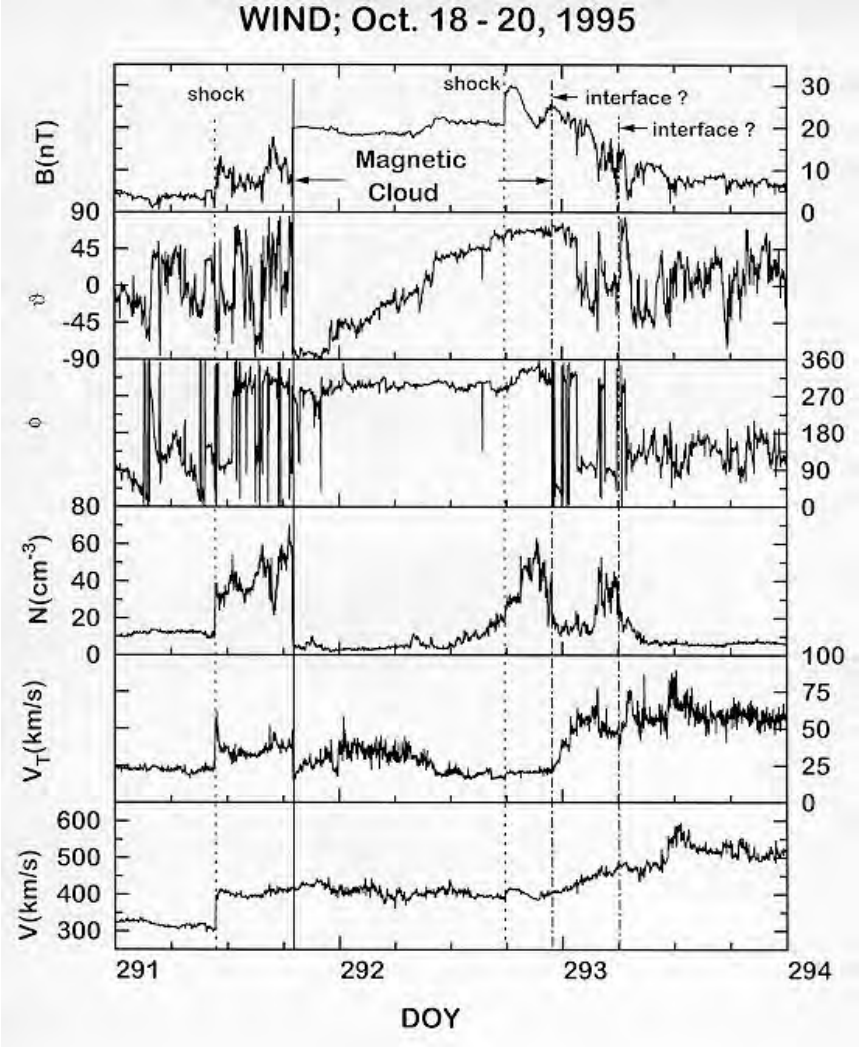

Figure 2.8: IMF and Solar wind parameters showing conditions for MC occurrence. From top to bottom: the IMF magnitude (B), the elevation (θ) and azimuth (φ) of the magnetic field vector, the proton density (N), the proton thermal speed (V_T) and the bulk velocity (V). Obtained from Lepping et al., 1997

MCs are one of the important space weather phenomena which can cause geomagnetic storms (Tsurutani et al., 1988; Zhang and Burlaga, 1988 and Wu and Lepping, 2002). The depression in horizontal component of the magnetic field which is caused by intensification of ring current is an important indicator of geomagnetic storm (Gonzalez et al., 1994). The severity of the storm is measured using the D_{st} index. A magnetic storm of $D_{st} < 100nT$ is caused by about $10nT$ southward component of IMF during MC (Gonzalez and Tsurutani, 1987 and Huttunen et al., 2005). However when the magnetic field is mainly northward the MC can be non-geoeffective and may not cause geomagnetic storm (Huttunen et al., 2005).

2.5 Effects of magnetic clouds

2.5.1 Radiation belt particle dropouts

As briefly mentioned in the previous chapter, radiation belts were first observed by van Allen in 1958 using spacecraft on board Geiger counter (Van Allen and Frank, 1959). The radiation belts are created from energetic particles which mainly originated from the Sun and are trapped in the magnetic field of the Earth. The shape and the dynamics of the magnetometer, which is greatly influenced by the solar wind, dictates the motion of particles trapped in the field. As mention in chapter one, charged particle which is trapped in magnetic field undergoes gyro-motion, bounce motion and drift motion. If the magnetic field unchanged on a scales similar to the respective motion, the three periodic motions are associated with constants of motion which are referred to as adiabatic invariant (Chen and von Goeler, 1985).

The particle flux in the radiation belt found to dropout during geomagnetic storms. It was perceived that the observed flux variations were totally linked to adiabatic invariant. However, both adiabatic and non-adiabatic changes occur in the course of particles flux variations (Turner et al., 2012). The adiabatic response is related to the D_{st} effect where the flux variation completely recovers after the main phase of the geomagnetic storm or upon the withdrawal of external driving force. The non-adiabatic response related to solar wind magnetospheric coupling where flux dropouts do not recover after the main phase of geomagnetic storm, in which the particle loss is irreversible (Onsager et al., 2002 and Green and Kivelson, 2004). Phenomena like magnetic clouds, solar wind streams and corotating interaction regions (CIR) exhibit solar wind conditions that cause geomagnetism storms which leads to irreversible flux dropouts.

Though the geomagnetic storms are known cause of irreversible dropouts, a study using a complete solar cycle data demonstrated that only about one quarter of more than 250 storms actually resulted to flux decreases (Reeves et al., 2003). The effective losses can be to the magnetopause or to the atmosphere and consequently to the middle atmosphere. The loss to the magnetopause is associated with intensification of solar wind dynamic pressure due to a rapid outward radial transport (Turner et al., 2012) while the loss to the atmospheric precipitation is due to pitch-angle scattering through wave-particle interaction (Green et al., 2004 and Millan and Thorne, 2007). The losses to the atmosphere can be identified directly from the observation of precipitation flux and from large decreases in outer zone trapped fluxes (Xiang et al., 2016).

2.5.2 Energetic particle precipitation

Energetic particles of different origins precipitate into the Earth and have many complex influence in the atmospheric processes (Bazilevskaya et al., 2008). The Sun continuously blows solar wind containing energetic charged and magnetized particles directly to the Earth. These particles and energy are trapped in the Earth's magnetic field and when upon released they attend enormous acceleration to create the aurora and radiation belt participles. During geomagnetic storms these particles and energies access the atmosphere.

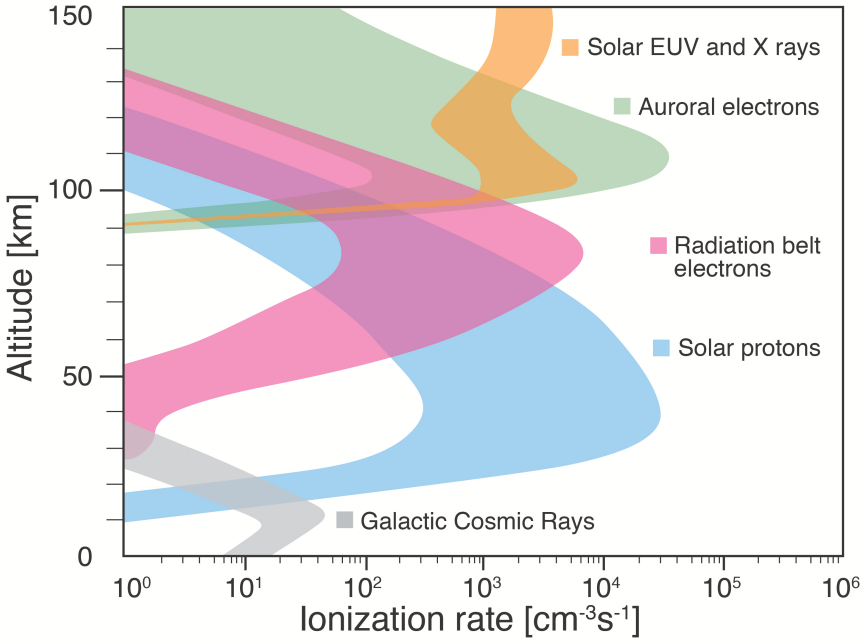

Figure 2.9: Instantaneous ionization rates of EPP, Solar EUV and X-ray of the Earth's atmospheric layers. Obtained from Mironova et al., 2015.

Particle precipitation to the atmosphere is an important relation between the Van Allen radiation belts and the Earth's atmosphere. Figure 2.10 shows a map of the precipitating $>$ 300 keV electron fluxes for on 31 May 2013 as measured by the NASA POES mission over Southern Hemisphere which shows particle precipitations in the region including the middle latitude.

Particle precipitation to the atmosphere from the radiation belt during geomagnetic activity is mainly caused by high-speed solar wind stream or magnetic clouds. The response of the atmosphere to particles precipitation from the radiation belts are studied for a possible link to climate variation among many other things. The very prominent response of the atmosphere due to energetic particles participation is ionization of neutral molecules such as N_2 and O_2. The odd nitrogen (NO_x) and odd

hydrogen (HO_x) are results of ionization by precipitation of energetic particles into the atmosphere (Rusch et al., 1981; Randall et al.; 2007; Turunen et al., 2009).

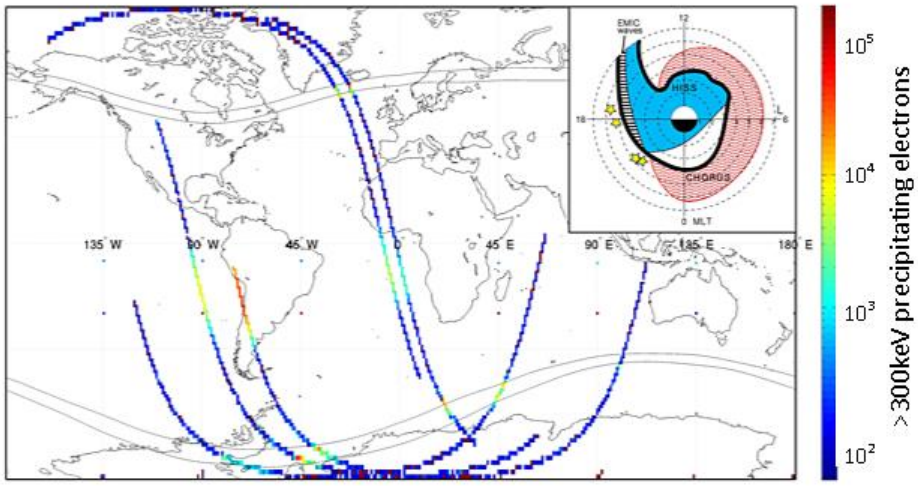

Figure 2.10: A map of the orbits color scale represents of > 300keV precipitating electron flux of POES during 21:1522:00 UT on 31 May 2013. Obtained from Clilverd et al., 2015.

The further reaction mostly depends on the lifetime reactive nitrogen and hydrogen. The HO_x is short-lived and highly localized as a result, it is observed only where the ionization occurs whereas the NO_x is long-lived, specially those created in the night side, can be transported to the stratosphere and react with the ozone (Solomon et al., 1982). The reaction degrade ozone which can reduce absorption of radiation (Seppälä et al., 2004). The energetic particles production of reactive nitrogen more frequent than production solar proton event. Solar proton events occur during CME when huge mass of plasma which is dominated by protons ejected into interplanetary space. These events may enhance proton flux in the atmosphere. Solar proton events are mostly observed in the polar cap regions poleward of $\sim 60^o$ geomagnetic latitude. The effect can expand further to mid-latitude during large solar proton events. Large solar proton events can have a great impact on the middle atmosphere but their occurrence is rare (Sinnhuber et al., 2012). The list of all solar proton events since 1976 can be obtained from NOAA website of space environment service center at https://umbra.nascom.nasa.gov/SEP/ which lists all solar proton events affecting the Earth environment as measured by GOES spacecraft. Other related effect resulted from ionization is electron density increases in the ionosphere which greatly impact the ionospheric convectional and currents.

Studies show that the solar activities which include electromagnetic radiations such as from solar flares, auroral particles, solar energetic particles, radiation belts particles and galactic cosmic radiation have significant impact on the upper atmosphere

(Rosenberg et al., 1979 and Danilov and Lastovicka, 2001). The effects of these inputs into the atmosphere are heating and ionization. As part of solar activity magnetic clouds effectively causing geomagnetic disturbance (Wang et al., 2003) can have important roles in the upper atmosphere. But, the effect in the lower and the middle atmosphere can be questionable and ambiguous (Herman and Goldberg, 1978).

It should be noted that a relation has been observed between the 11-year solar cycle, which is associated with sunspot numbers and surface temperature with different solar hemispherical effects (Labitzke and Loon, 1989; Georgieva et al., 2000). The helicity of magnetic structure which depends on differential rotation of the Sun (DeVore, 2000) found to be predominantly negative (left-handed) in the North and positive (right-handed) in the South (Antonucci et al., 1990). The possible statistical impact of MC on the middle atmosphere based on the geo-effectiveness of MC on the middle atmosphere showed by Georgieva et al. (2005). The study demonstrated that, MCs have an effect in the stratospheric dynamics and the effect depend on the direction of rotation of the magnetic field in the magnetic clouds as well as on the phase of the quasibiennial oscillation (QBO) of equatorial stratospheric winds. And the left-hand MCs found to have higher speed and cause greater magnetic disturbance in QBO Easterly phase both in Northern and Southern hemispheres. Based on a model calculation (Ogunjobi et al., 2014) estimated that energy deposition upon the arrival of MC event on 8 November 2004 increased to about the altitude of 100 km in the Northern hemisphere and to lower altitudes in Southern hemisphere.

The other possible method to observe the effect of MCs in the middle atmosphere is communication signal propagation. MCs are found to trigger large geomagnetic storms which allow particles precipitation into the atmosphere and related ionization. Ionization in the middle atmospheric due to energetic particle or electromagnetic wave penetration that affects the propagation of VLF signals (Vampola and Gorney, 1983) which have suggested that some of the neutral gas affected by variations in the middle atmospheric energy inputs which increases temperature.

2.5.3 Mid-latitude precipitation

According to Baker (2004), ions in the energy range 10 - 200 keV can precipitate onto mid-latitudes just from inside the plasmapause through the ring current. Foster et al. (1998) have observed such ions to be anisotropic and transport down to an altitude of about 120 km. The energy flux increases with magnetic disturbance. During magnetic disturbed conditions, the precipitating ions and neutrals are the primary source of nighttime ionisation at these altitudes and latitudes. Ring current ions

interact with the outer edge of the plasmasphere, where they excite ion cyclotron waves. These waves lead to scattering of the ring current ions, which most likely produces the observed precipitation. Outside the plasmapause there is another region of ion precipitation, where the observed precipitating flux is more isotropic. The filled loss cone suggests that a mechanism for outward radial diffusion and strong pitch angle scattering within the magnetosphere is in existence. Baker (2004) also noted the extension of magetospheric particles through the aurora zone to the mid-latitude.

Chapter 3

Data and instruments

This study uses both space-borne satellites and ground based instruments data. The multi-satellites database OMNIWeb, NOAA/POES and GOES satellites data were employed for this study. Data from ground based observations, ionosonde and magnetometer, are also used in this study. This Chapter describes all the instruments database used. Events selection and characterization also described in this Chapter.

3.1 Satellites data

3.1.1 OMNIWeb data

The OMNIWeb database is near-Earth solar wind, magnetic field and plasma parameter data compiled from a number of satellites (King and Papitashvili, 2005). These near-Earth observations are direct manifestations of near-Sun conditions. The dataset is produced by National Space Science Data Center (NSSDC) after extensively cross comparison, and, for few spacecraft and parameters, cross-normalization among satellites measurements. The data is available in hours, days and 27-days resolution from 1963 to the present day at http://omniweb.gsfc.nasa.gov. Starting from 1981 better resolution (1-minute and 5-minute) are available. Most of the tributaries of IMF and plasma measurements are delayed by several minutes due to geomagnetic bow shock (Weimer et al., 2002). To address this data mismatch, the measurements affected by the lag are mixed up with other closer-to-Earth satellite measurement before producing them into an hourly average dataset. The shift is determined statistically from a number of factors such as Earth's orbital rotation about the Sun and different solar wind behaviors.

Parameters used to study geomagnetic storms and magnetic clouds were acquired from OMNIWeb dataset. These parameters are the magnitude of interplanetary magnetic field (IMF) B_{mag}, z-component of IMF B_z, proton number density n_p, solar wind speed V_{SW}, alpha to proton ration n_α/n_p , solar wind pressure dynamics P_{dyn}, interplanetary magnetic storm index K_p, and geomagnetic storm time disturbance index D_{st}. All these parameters used here are hourly average except for K_p which is 3-hours averages.

3.1.2 GOES data

The Geostationary Operational Environmental Satellite (GOES) satellites do orbit the Earth in a geosynchronous orbit. There are a number of GOES satellites and their primary purpose is environmental observation of Earth atmosphere. In addition to their primary missions, detectors such as Energetic Proton, Electron and Alpha Detector (EPEAD) are also deployed on board GOES satellites. There are two EPEADs which have 3-electron ($>$ 0.8 MeV, $>$ 2.0 MeV and $>$ 4.0 MeV) and 7-proton (2.5 MeV, 6.5 MeV, 11.5 MeV, 30.6 MeV, 63.1 MeV 165 MeV and 433 Mev) channels on each satellites (GOES 13, GOES 14 and GOES 15). One detector has east field-of-view and the other has west field-of-view (Onsager et al., 1996).

The GOES data is available in 1 minute and 5 minutes average on NOAA website http://satdat.ngdc.noaa.gov/sem/goes/. In this study hourly average was used in order to compare with OMNIWeb dataset. All the available GOES data are incorporated for the mean estimation, that is in 2014 and 2015, GOES 13 and GOES 15, and in 2016 GOES 13, GOES 14 and GOES 15. Here, GOES measurement employed to observe energetic particles loss from the radiation belt by MC events.

3.1.3 POES data

National Oceanic and Atmospheric Administration/Polar Orbiting Environmental Satellites (NOAA/POES) are polar-orbiting, Sun-synchronous, low-altitude (about 850 km) satellites. Their period is about 100 minutes, that means they are fast and can orbit 14 to 15 times in one day. Like GOES, the primarily purpose of POES is Earth's environmental observation of the atmosphere. In addition, the Medium Energy Proton and Electron Detector (MEPED) and Total Energy Detector (TED) on board POES/MetOp (Evans and Greer, 2000). The MEPED on each satellite have 0^o telescope which measures precipitation and 90^o telescope which measures trapped energetic particles. The energetic particles (electrons and protons) are measured separately, however, the electrons measurements are found to have proton contamination

(Rodger et al., 2010). A correction method, first order, should be employed to suppress proton contamination for accurate electrons measurement (Lam et al., 2010). To obtain accurate particle precipitation measurements, data from 0^o telescope when only measures particles inside the loss cone are considered. This can be effectively applied in the first adiabatic invariant to determine the local pitch angle at satellite that corresponds to the edge of the loss cone α_{satLC} which is given by

$$\alpha_{satLC} = \sin^{-1}(\sqrt{\frac{B_{sat}}{B_{120}}}) \tag{3.1}$$

where B_{sat} is the ambient magnetic field at the satellite and B_{120} is the ambient magnetic field of the foot of the field line approximately at 120 km altitude above the Earth. The magnetic fields can be calculated using the International Geomagnetic Reference Field (IGRF). The MEPED field of view is 30^o ($\pm 15^o$) for precipitating particles, hence

$$\alpha_{sat} + 15^o < \alpha_{satLC} \tag{3.2}$$

where α_{sat} is the particle pitch angle at the satellite. For the 0^o telescope the field of view lies within the bounce loss cone for $L > 1.4$ (Rodger et al., 2010). All the active POES satellite data is used in this study to estimates temporal variation of precipitating particles flux. At least one of the satellite provides measurement of a region of interest. In 2014 POES-15, POES-16, POES-18, POES-19, POES-m01, and POES-m02 are used. In 2015 and 2016 POES-15, POES-18, POES-19, POES-m01, and POES-m02 are used to generate the dataset. Figure 3.1 shows the footprint of different POES satellites as passing the Northern and Southern hemispheres. The data can be downloaded from NOAA website at http://poes.ngdc.noaa.gov/data/.

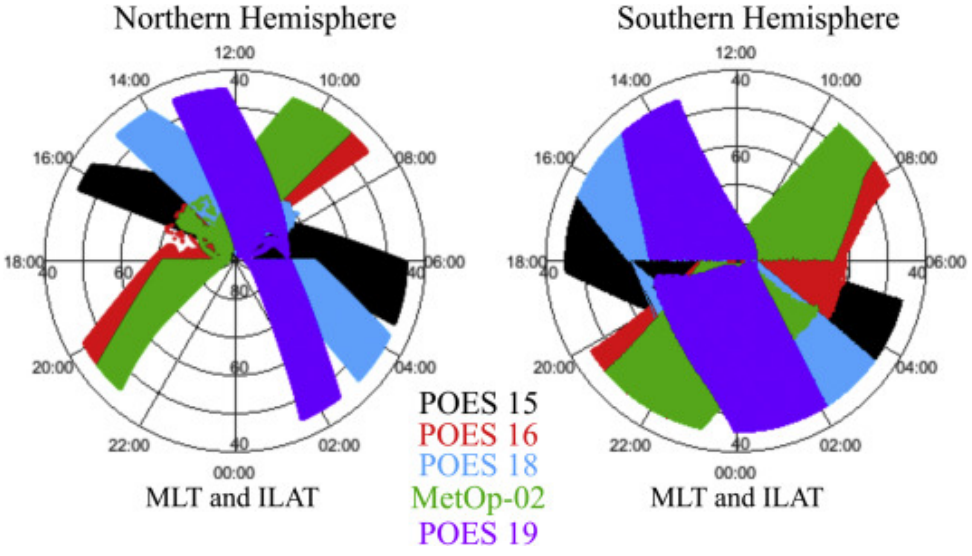

Figure 3.1: The footprint of the different NOAA/POES satellites in the Northern and Southern hemisphere. Obtained from from Søraas et al., 2017.

3.2 Ground based data

3.2.1 Ionosonde data

Ionosonde is a low power ($\sim$ 10 kW) vertical sounding radar that operates within a frequency range of 0.1 MHz to 40 MHz (Davies, 1990). It is a ground based instruments and used to measure the ionosphere from the bottom-side approximately up to 400 km from the ground. A number of ionosonde are required for wider spacial coverage because as it is a localized instrument and provide measurements at a particular location. Short pulse HF signals are transmitted into the ionosphere (Figure 3.2). The ionosphere reflects the signals back to the ground and ionosonde records the time delay between the transmission and reception. The vertical range of the wave reflection, the height is given by,

$$h = \frac{c\tau}{2} \tag{3.3}$$

where c is the speed of the electromagnetic wave and τ is the time delay. Using Appleton-Hartree equation, the plasma frequency can be calculated and is given by,

$$\omega_p = \sqrt{\frac{Ne^2}{\epsilon_o m}} \tag{3.4}$$

where ω_p is angular plasma frequency, N is electron number density, e is charge of electron, m is mass of electron and ϵ_o is constant.

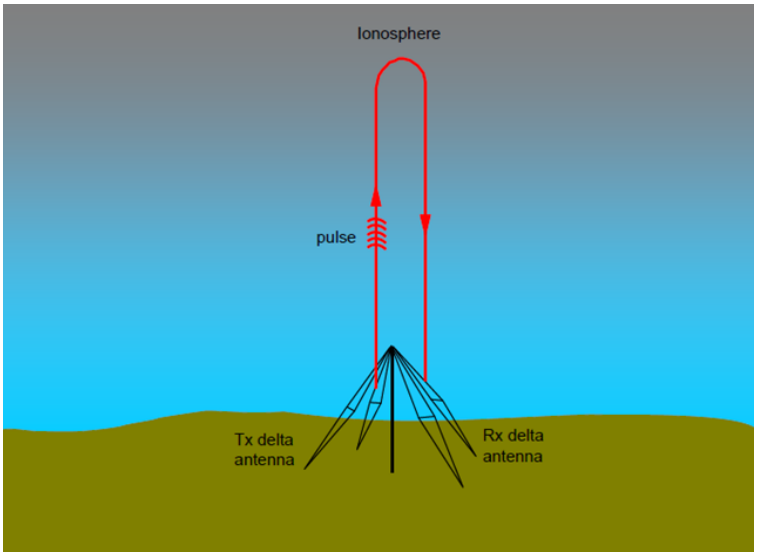

Figure 3.2: Schematic Diagram of ionosonde showing transmitted and received signals. Obtained from http://www.sws.bom.gov.au/Educational/5/2/2. Accessed on 20 May 2017.

In this study the South African ionosonde data was employed to observe how the lower ionosphere responded during geomagnetic storm driven by magnetic clouds. There are four ionosonde stations in South Africa, the names, locations and their corresponding statuses are given in Table 3.1.

Table 3.1: List of ionosonde stations in South Africa. Obtained from http://spaceweather.hmo.ac.za/index.php?action=info&topic=IONOSONDE. Accessed on 18 December 2017

Station	Latitude(°)	Longitude(°)	Start Date	Status
Hermanus	-34.4	19.2	August 2008	working
Grahamstown	-33.4	26.5	January 1973	working
Louisvale	-28.5	21.2	August 2000	working
Madimbo	-22.4	30.9	August 2000	no data since 2012

Figure 3.3 shows range variations of different measured and calculated variables of the ionogram display of Hermanus station. The black solid line shows the computed electron density profile over the true height. The red and green points show locus of received ordinary and extraordinary frequencies respectively and corresponding vertical ranges. The light blue points indicate ionospheric reflection from the North-Northeast section. The points at the top of the plot indicate second time reflection (double hop) of ordinary and extraordinary frequencies corresponding to the vertical ranges.

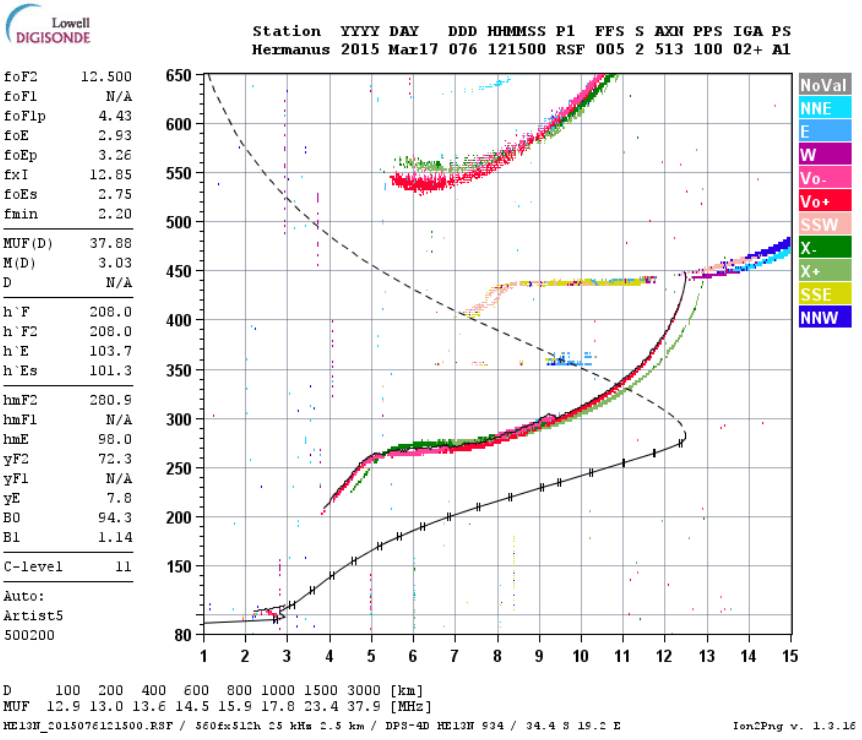

Figure 3.3: Ionogram showing electron density and frequency against height 17 March 2015, 12:15:00 UT. Obtained from SANSA ionosonde dataset 2015

In this study the ranges and critical frequencies of E-layer and Es-layer, which are the lower ionosphere that corresponds to MLT, are investigated.

3.2.2 Magnetometer data

Ground based magnetometers are used to measure perturbations of the Earth's magnetic field. Ground based magnetometers are one of the most important magnetosphere-ionosphere coupling measurements. Important geomagnetic parameters such as K_p, AE and D_{st} which are used to scale magnetic storms and geomagnetic disturbance are derived from ground based magnetometers (Gonzalez et al., 1994). A magnetic field is described by the magnetic field vector. The magnetic field vector is characterized by its direction and flux density. The observations of magnetic field can be done by measuring charges in the magnetic flux or in atomic level by applying the atoms behavior of substances in a magnetic field, such as proton procession or Zeeman effect (May-Britt, 2001).

A worldwide collaboration of organizations and national agencies for ground based magnetometer data is called SuperMAG. SuperMAG provides easy access to validated ground magnetic field temporal variation measurement in the same coordinate system, identical time resolution and with a common baseline removal approach (Gjerloev, 2012). The purpose of SuperMAG is to assist all ground magnetometer data users with easy access to measurements of the Earth's magnetic field. South Africa has two magnetometer stations which are part of SuperMAG. The magnetometer data can be obtained from SuperMAG website at http://supermag.jhuapl.edu. In this study the South African magnetometer data (Hermanus and Hartebeesthoek stations) are employed during magnetic cloud events to evaluate how ground magnetic field changed and possibly affect the local lower ionosphere. The SuperMAG data is one minute average and the hourly mean are calculated to produce a dataset as in other instruments dataset.

3.3 Events selection and characterization

Extreme magnetic storms at the Sun active region, which cause extreme geomagnetic storms, erupt and eject a large volume of coronal materials called coronal mass ejections (CMEs). The list of near-Earth interplanetary coronal mass ejections (ICME) were taken from *www.srl.caltach.edu/ACE/ASC/level3/icmetable2.html*. These lists of ICMEs are manifestations of the coronal mass ejection near the Sun as observed by coronagraph and characterized using geophysical observation (Richardson and Cane,

2010). MC can be identified inferring geomagnetic parameters and solar wind conditions which show high magnetic field magnitudes, low ratio of plasma to magnetic pressure, low proton temperature, and smooth rotation of the magnetic field vector. Most of the listed ICMEs are associated with magnetic cloud (MC) events, but for this work only those showing strong magnetic cloud features have been selected to study their effect in the middle atmosphere. Table 3.2 lists the selected ICME event dates which show strong MC features with their respective magnitude of magnetic field and minimum value of D_{st} index. This is because any effect of geomagnetic storm over our region of interest, which is South Africa (midlatitude), require perturbation of region current

Table 3.2: List of selected ICME event dates.

ICME Event date	IMF magnitude	Dst index
29 April 2014	10 nT	-60
17 March 2015	30 nT	-223
31 December 2015	16 nT	-110
13 October 2016	24 nT	-104

In 2014 twenty ICME events are listed of which about nine of them are indicated to show clear features of MC and event on 29 April 2014 is selected. In 2015 thirty ICME events are listed of which about eleven of them are indicated to show clear features of MC and events on 17 March 2015 and on 31 December 2015 are selected. In 2016 thirteen ICME events are listed of which about seven of them indicated to show clear features of MC and event on 13 October 2016 is selected.

The magnetic cloud events, as one the triggers of extreme geomagnetic events, can be identified as an inferring geomagnetic and solar wind parameters which show high magnetic field magnitudes, low ratio of plasma to magnetic pressure, low proton temperature, and smooth rotation of the magnetic field vector in a period of the order of one day observed as the spacecraft passes through it (Burlaga et al., 1981 and Huttunen et al., 2005).

Chapter 4

Energetic particle dropouts

4.1 Case 1: MC event of 29 April 2014

4.1.1 Geophysical properties

The measurements of geophysical and solar wind conditions were examined for the selected events from OMNI database (*https://omniweb.gsfc.nasa.gov/form/dx1.html*). The OMNI hourly database provides near-Earth solar wind, magnetic field, and plasma parameters observations from a number of spacecraft in geocentric orbits. The dataset is created by National Space Science Data Center (NSSDC) after extensively cross compared and normalized (King and Papitashvili, 2005). Hence, this dataset is an important tool to identify the MCs and characterize the geomagnetic storms that MCs may trigger (Burlaga et al., 1982).

Figure 4.1 presents the temporal variation of geophysical and solar wind parameters between 25 April and 05 May 2014 of MC occurred on 29 April 2014 indicated by the dotted vertical lines using OMNIWeb hourly data. Figure 4.1 (a) shows the magnitude of IMF in geocentric solar magnetospheric (GSM) coordinates on the arrival of MC. As can be seen total IMF peaks about 10 nT at event onset. The smooth rotation of the z-component of the magnetic field from Southward to Northward indicates the arrival of MC as seen in (Figure 4.1 (b)) at Earth bow shock nose (1AU). Prior to the MC arrival IMF is weak (passive) and gradually reverses to negative (about -9.4 nT) on MC arrival. The maximum magnitude of magnetic field strength coincides with the minimum of its z-component indicates enhanced magnetic activity.

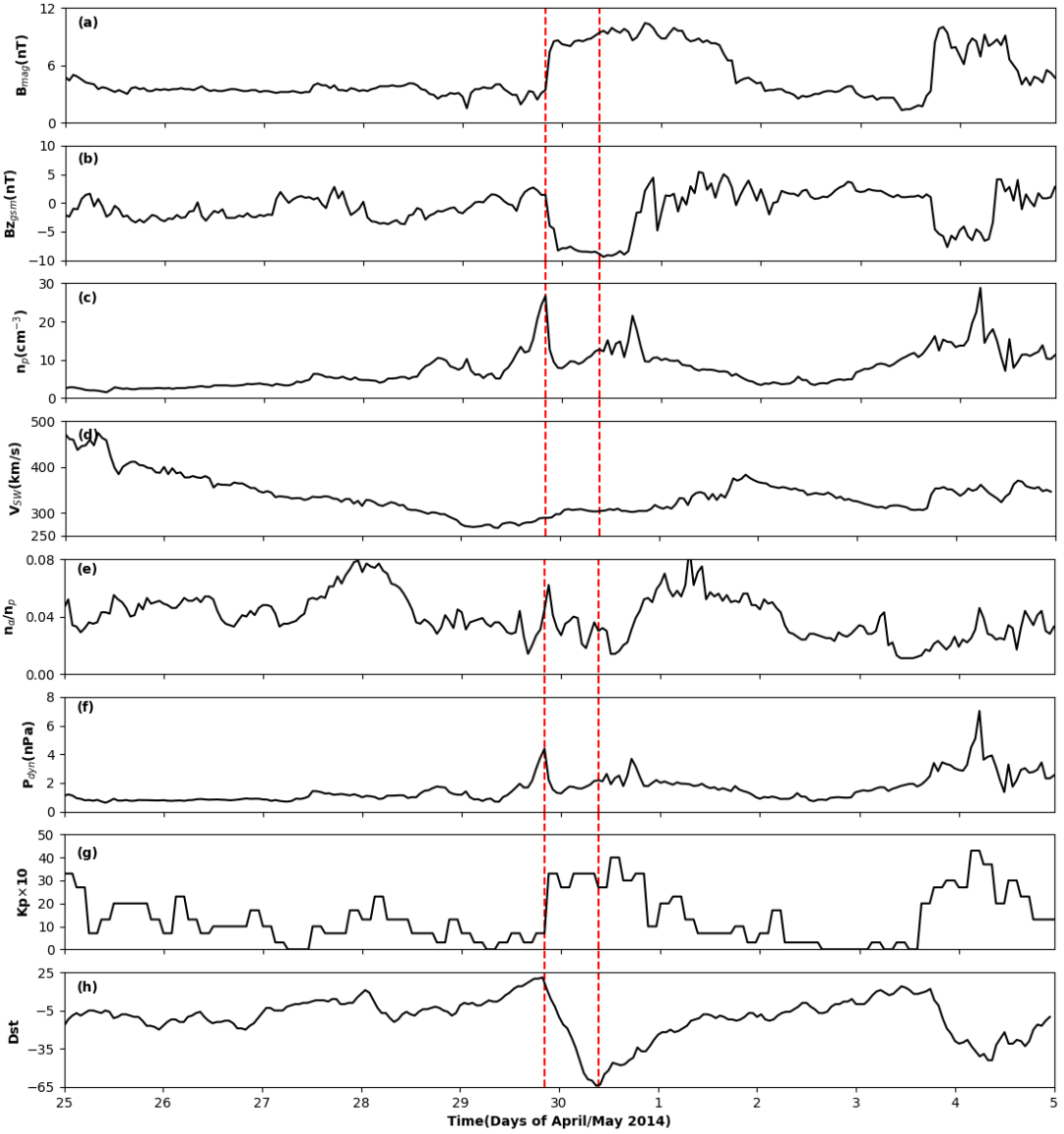

Figure 4.1: Plots of geophysical and solar wind conditions of MC event on 29 April 2014: panels (a) show IMF magnitude, (b) z-component of IMF in GSM coordinate, (c) proton number density, (d) solar wind speed, (e) alpha to proton ratio (n_α/n_p), (f) dynamic pressure, (g) K_p index, (h) D_{st} index in OMNI hourly format. The vertical dotted lines indicates MC interval north-south.

The plasma number density sharp increases to above 25 cm^{-3} and immediately decreases to bellow 10 cm^{-3} onset (Figure 4.1 (c)). The solar wind (Figure 4.1 (d)) shows to rise at the event arrival which indicates geomagnetic actively. The solar wind continues to rise from about 250 km/s to about 383 km/s three days after the event. Figure 4.1 (e) presents the alpha proton ration which shows that the alpha proton ratio is low at event onset. The alpha proton ratio drops from 0.04 to about 0.02 at event onset. It gradually reverses to previous level. The solar wind dynamic

pressure (Figure 4.1 (f)) decreases prior and after the event arrival. At the event arrival dynamic pressure increases.

A magnetic storm is confirmed by development of K_p index to +4 (Figure 4.1 (g)) which shows relatively high magnetospheric activity. Prior to the event time the magnetospharic convention is low and peak to about 40 nT on arrival as shown in Figure 4.1 (g). This continues for two days after the event. At this time of enhanced magnetospheric activity, the ring current is expected to be intensified. The robust negative D_{st} index value (Figure 4.1 (h)) shows ring current decay. As can be seen, D_{st} depressed to about -65 nT at event onset. This relative high to what observed prior the event (about zero nT). The sharp northword value at event onset indicate calm before storm (Ogunjobi et al., 2014) which can be seen in Figure 4.1 (b). The disturbance on 4^{th} of May perhaps caused by interplanetary magnetic shock rather than MC confirmed from relatively high K_p index and small D_{st} depression ($<$ -50 nT). When the MC occurs, it triggers geomagnetic storm or alternatively will couse energetic particles dropouts from the radiation belt. The MC triggered storms compress the magnetosphere towards the Earth, which may allow loss particles to access the middle atmosphere and affect its composition and temperature (Ogunjobi et al., 2014).

4.1.2 Particle dropouts

The particle dropouts from the radiation belt can be both adiabatic and non-adiabatic in which solar wind conditions play a major role. The mechanism of loss with its energy dependencies on the dropout ranges in L-value and effective duration in time as well the recovery of the radiation belt have been reported in the literature (Onsager et al., 1996, Turner et al., 2012 and 2014). Here in this study, the temporal variation of particles using the GOES particles flux data during MC events is employs to examine particle dropouts. The GOES data is available in 1 minute and 5 minutes average on NOAA website. In this study, the hourly average was employed in order to compare with the available resolution used in section 4.1. This helps to observe how the geophysical properties are related with the particle dropout from radiation belt during MC.

Figure 4.2 shows hourly averaged observations of radiation belt particles fluxes at the geostationary orbit by GOES satellites. Figure 4.2 (a) and (b) show a remarkable sudden electron flux dropout at $>$ 0.8 MeV and $>$ 2 MeV channels of both GOES-13 and GOES-15 respectively. The time of the flux dropout coincides with the MC shown by the dotted vertical lines and the flux decreased substantially by about 3

orders of magnitude for both channels. This shows the dropout is significant and most likely related to the magnetic disturbance resulted from the interaction of MC with magnetosphere. The dropouts on the 4^{th} of April related to interplanetary magnetic shock rather than MC confirmed from relatively high K_p index and small D_{st} depression (Figure 4.1).

Figure 4.2 (c) shows that both $>$ 10 MeV and $>$ 30 MeV of protons flux do not show any significant change on the arrival and subsequent time of interaction of MC with the magnetosphere. Since dropout is energy dependent according to Onsager et al. (2002), the particular event could, perhaps, not act on the available proton energy at the onset. Although large magnetic storms are strongly related to solar proton events and during solar proton events the ejected plasma from the Sun is dominated by protons and when the event is large the mid-latitude region can also be affected (Sinnhuber et al., 2012). Therefore, it could also be that this is not strong enough to act on the available GOES proton channels.

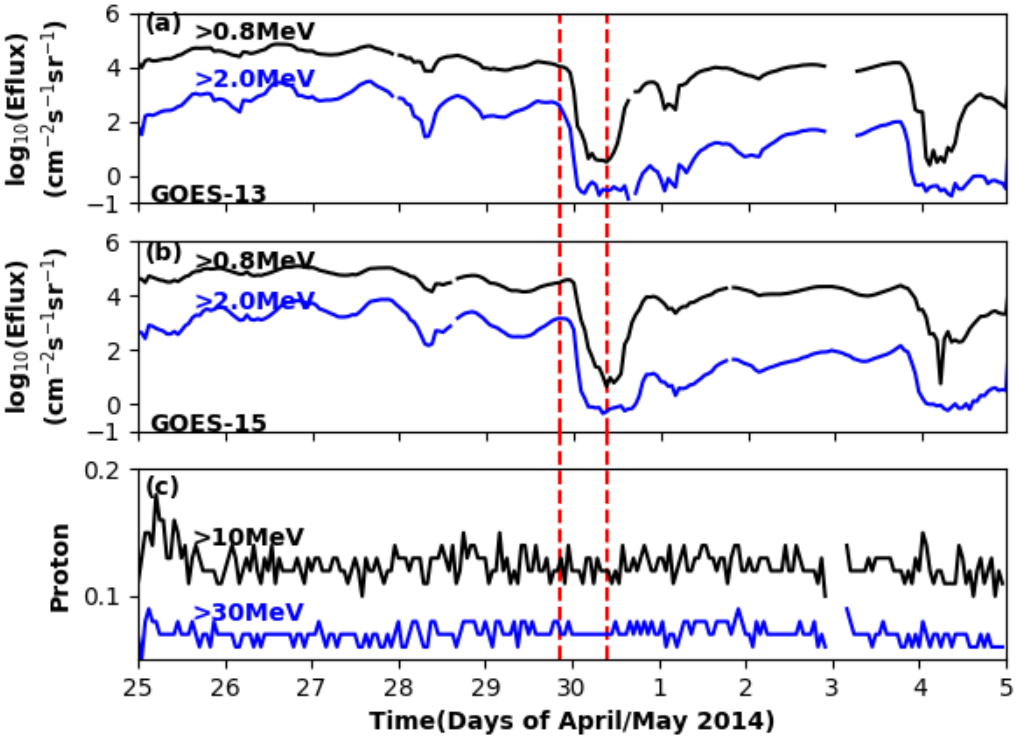

Figure 4.2: GOES particle flux measurement of MC-driven dropout of 29 April 2014. Panels (a) GOES-13 electron, (b) GOES-15 electron (the black curve is for $>$ 0.8 MeV and blue curve is for $>$ 2.0 MeV in (a) and (b)), and (c) GOES proton the black curve is for $>$ 10 MeV and blue curve is for $>$ 30 MeV. The vertical dotted lines indicate the MC interval.

4.1.3 Particle precipitation

The NOAA/POES particles data from MEPED instruments are employed to estimate particles precipitation when MC hits the Earth's magnetosphere. The POES satellite, as a LEO satellite can measure particles in the LEO such as particles that are lost from radiation belt and precipitate to the atmosphere in general (Evans and Greer, 2000). In order to examine energetic participles input to the atmosphere, only data from 0^o detectors of all available POES instruments are used in this analysis to obtain the precipitation over and near our region of interest. The particles measurements are projected down to about 100 km which is near the foot of the magnetic field lines and sorted in McIlwain L shell or latitude and longitude (Ogunjobi et al., 2014).

The region of interest, South Africa, is situated in the middle latitude geographically between 22^oS and 35^oS. Particle precipitation in $\pm 10^o$ the South African latitude is considered for the estimation. The estimation has been taken into consideration when the satellites measure this region to observe possible effect. The data is arranged in hours for concatenation of data from all available POES instruments and finally averaged hourly.

Figure 4.3 presents the proton flux in energy channel $\backsim$ 39 keV and the electron flux in energy channel $>$ 40 keV. The proton flux peaks, Figure 4.3 (a) at the MC arrival which shows that particle dropout is energy dependant. Even though we did not observe dropouts at the energy channels considered in Figure 4.3 (c) the lower energy channels could have shown significant dropouts. The trend in Figure 4.3 (a) provide truth to this. At event onset, the precipitation of $\backsim$ 39 keV proton energy peaks and return to pre-event level after the event. This provides a good indication that lower energy proton in deed dropout from the trapped radiation belt. Figure 4.3 (b) shows the relative enhancement of electron flux on MC arrival.

This particle precipitated into the atmosphere may have its own role, in complex multiple processes of the middle atmosphere, to contribute for the energy balance and composition. One of the important responses of the middle atmosphere or ionosphere to geomagnetic storm is minor component composition such as odd nitrogen and hydrogen (Turunen et al., 2009), changes as a result of energetic particle impact on the the middle atmosphere which both contribute to ozone depletion in the atmosphere and related temperature variations. The coupling of chemical composition changes and propagation from the source region where composition change occurs can affect the dynamics of the atmosphere and atmospheric heating and cooling. Hence, there is a clear evidence of MC triggered electron precipitation over South African middle atmosphere.

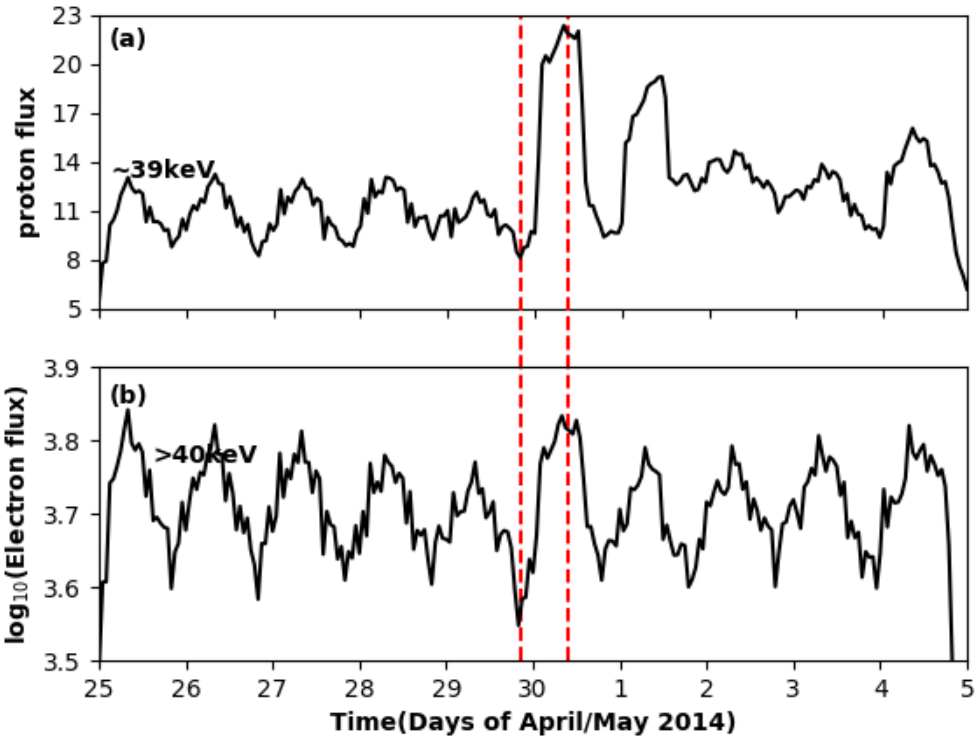

Figure 4.3: NOAA/POES particle precipitation measurement during MC of 29 April 2014. (a) shows ∽ 39 keV protons and (b) > 40 keV. The vertical dotted lines indicate the MC interval.

4.2 Case 2: MC event of 17 March 2015

4.2.1 Geophysical properties

This geomagnetic storm date was studied by Pierrand and Rosson (2016) using EPT/PROBA-V data for radiation belt particles dropouts. They reported that the injection of particles in the inner belt after geomagnetic storms were very significant and make the inner belt visible at all longitude at 820 km which shows the particle dropouts from the outer radiation belt to the atmosphere in general was large. The magnetic storm event on 17 March 2015 is specially interesting because it is the biggest geomagnetic storm date, with D_{st} index of -223 nT and K_p index of +7, in the current solar cycle thus far. The data analysis procedure and the format of presentations are similar to that presented in Section (4.1.1). Similar to Case 1 presented in section 4.1.1, we examine an other MC-trigger dropouts that occurs on

17 March 2015. This configuration will allow systemic configuration of precipitation seen in Case 1, particularly for the electrons.

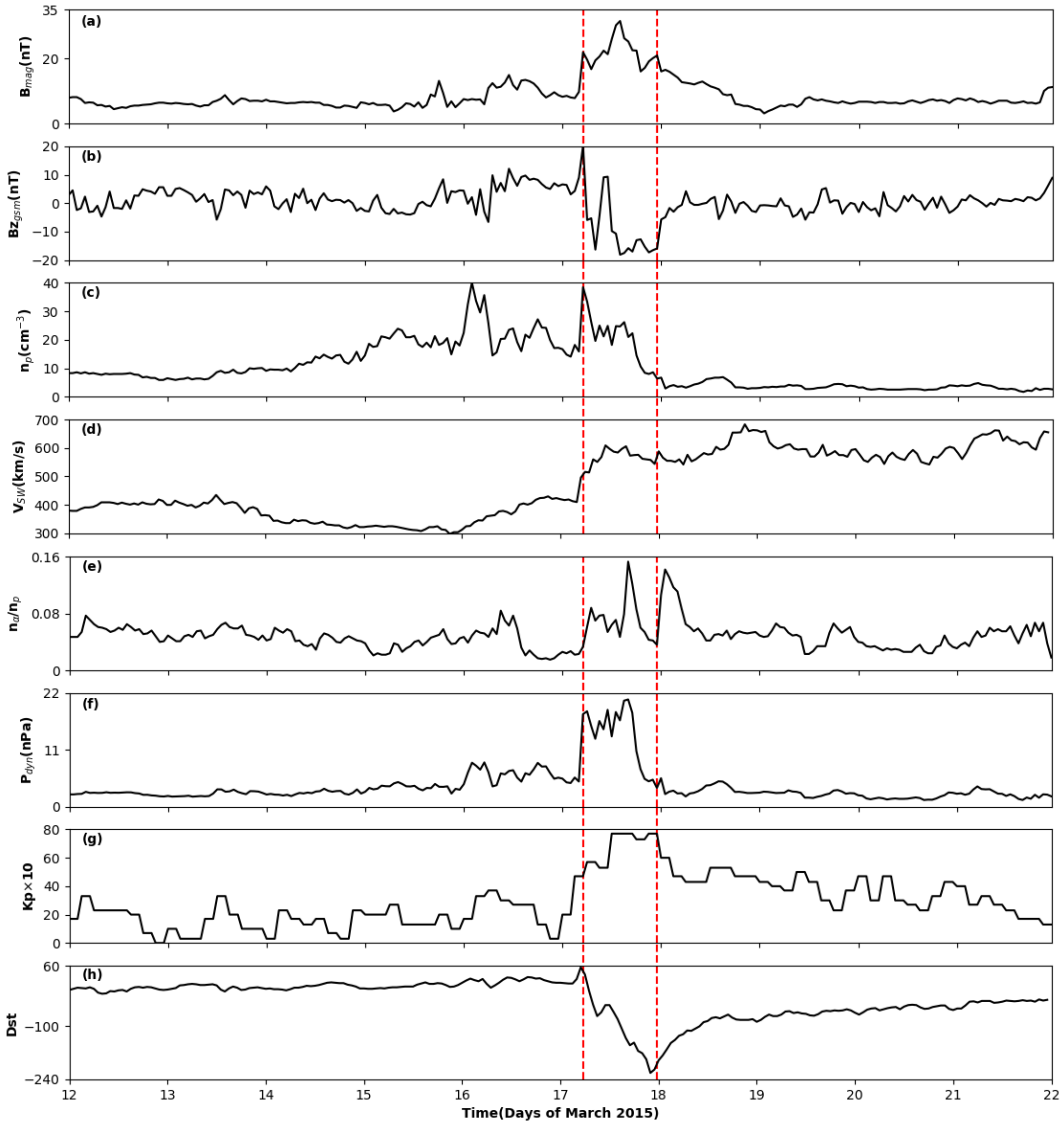

Figure 4.4: Geophysical parameters and solar wind conditions of MC on 17 March 2015. The format is same as in Figure 4.1.

The magnitude of IMF reaches 30 nT as shown in Figure 4.4 (a) on MC onset. The z-component of the IMF (Figure 4.4 (b)) oscillated and decreases to about -18 nT. The plasma number density also decreases at onset of MC (Figure 4.4 (c)). Figure 4.4 (d) shows a sudden increase of solar wind speed to above 600 km/s on 17 March and further increase to above 650 km/s in the last hours on 18$^{\text{th}}$ of March. The alpha proton ration fluctuates reaching to about 0.16 and back to about 0.04 as shown in Figure 4.4 (e) which indicates a disturbance onset the MC. The solar wind dynamic

pressure increases and for a while and decreases (Figure 4.4 (f)) as the storm passes. The shock caused an enhanced magnetospheric convention as observed in a high K_p index of +7 (Figure 4.4 (g)) as well as D_{st} index of -223 nT (Figure 4.4 (h)) which show intensification of ring current. The geophysical properties clearly demonstrate characteristics of MC followed by strong magnetospheric activity, similar to Case 1.

4.2.2 Particle dropouts

Figure 4.5 shows the response of radiation belt particles as measured by GOES satellites. The format of pretension is the same as in Section 4.1.2. Figure 4.5 (a) and (b) confirm that the flux dropout occurred for the electron energy channels of > 0.8 MeV and > 2.0 MeV of both GOES-13 and GOES-15, respectively. The time of the flux dropout coincides with the MC as shown by two dotted vertical lines and the flux decreased substantially by about 2 orders of magnitude for both channels. The temporal variation shows fluctuation in the time of MC, perhaps this is due to the north to south fluctuation of the IMF B_z. After the MC passed in later days specially for > 0.8 MeV, the flux increased beyond the flux before the MC date and this perhaps related to strongly enhanced substorm activities ejecting back electron population at the early stage, which subsequently under gone efficient loss processes to account for substantial drops in the electron flux (Xiang et al., 2016).

This shows that the dropout is significant and most likely related to the magnetic disturbance resulted from the interaction of MC with magnetosphere rather than adiabatic variations. The recall that adiabatic variation is a local effect, the recovery of dropout is also prolong and did not return with IMF B_z. This further confirm true loss of electron from the trapped radiation belt. The protons flux of > 10 MeV, Figure 4.5 (c), depleted completely as MC interact the magnetosphere while > 30 MeV protons show no signification change. This further confirm our previous observation in Case 1. The higher the magentospheric convention, the higher the energy of dropouts. Relatively small electrons dropouts on 12 March and 15 March could be related to small magnetospheric fluctuation (See Figure 4.4) and other phenomena such as substorm in which a brief magnetosphreic disturbance from the tail release and drive energy. The proton dropout for this particular event is significant because the magnetic storm caused by MC is large compared to the geomagnetic event on 29 April 2014.

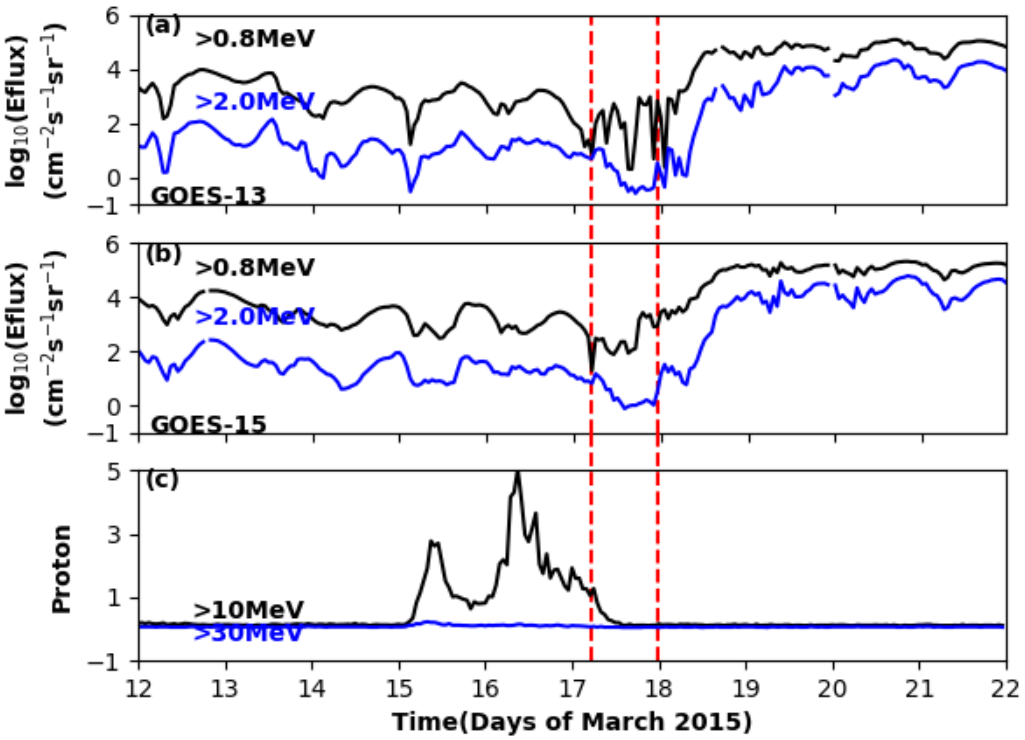

Figure 4.5: Particle flux measured by GOES satellites during MC-driven dropout of 17 March 2015. The format is as in Figure 4.2.

4.2.3 Particle precipitation

Figure 4.6 presents the POES proton flux in energy channel $\backsim$ 39 keV and electron flux in energy channel $>$ 40 keV to show particles precipitation in our region of interest. The format of presentation is the same as in Section 4.1.3. The proton shows peak (see Figure 4.6 (a)) after the MC arrival which shows the significant increase in proton flux coincides with the MC and flux change related to the radiation belt particles dropouts. This further affirms our previous observation as presented in Section 4.1.3.

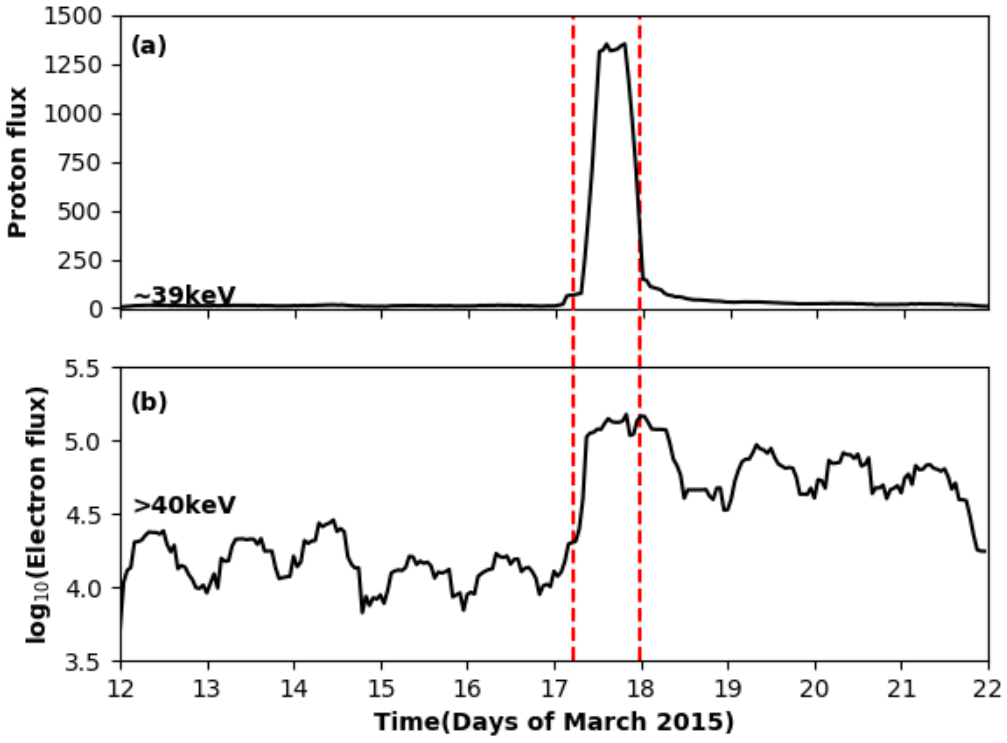

Figure 4.6: NOAA/POES particle precipitation on the arrival of MC on 17 Marc. (a) shows ∽ 39 keV protons and (b) > 40 keV. The format is same as in Figure 4.3.

4.3 Case 3: MC event of 31 December 2015

4.3.1 Geophysical Properties

An other study of MC event is presented. Here we present MC event that cover both day and night (a broader time interval). Similar to that presented in Section (4.1.1), Figure 4.7 illustrates the geophysical parameters of MC that occurred between 26 December 2015 and 5 January 2016. Similar to Case 1 and Case 2, the IMF magnitude enhanced to about 16nT (Figure 4.7 (a)) and the z-component of the IMF(Figure 4.7 (b)) oscillated and went below -15 nT. The maximum of IMF and minimum of its z-component coincide. Panels (a) and (b) show the enhanced total IMF and the depressed z-component of IMF with smooth rotation to southward respectively while the plasma number density decreases at onset of MC (Figure 4.7 (c)). Figure 4.7 (d) shows that solar speed decreasing from its peak on 27th December (which shows some activity prior to this time) and sudden increase above 480km/s on 31th December and persisted almost the same speed. The solar wind dynamic

pressure increases and for a while and decreases (Figure 4.7 (f)) as the storm passes. The shock caused geomagnetic storm which are observed in a high K_p index of +6 (Figure 4.7 (g)) and a low D_{st} index of -110nT (Figure 4.7 (h)) which again indicates the intensification of ring current. The inspection of geophysical properties clearly shows the characteristics of MC and attendant geomagnetic activity.

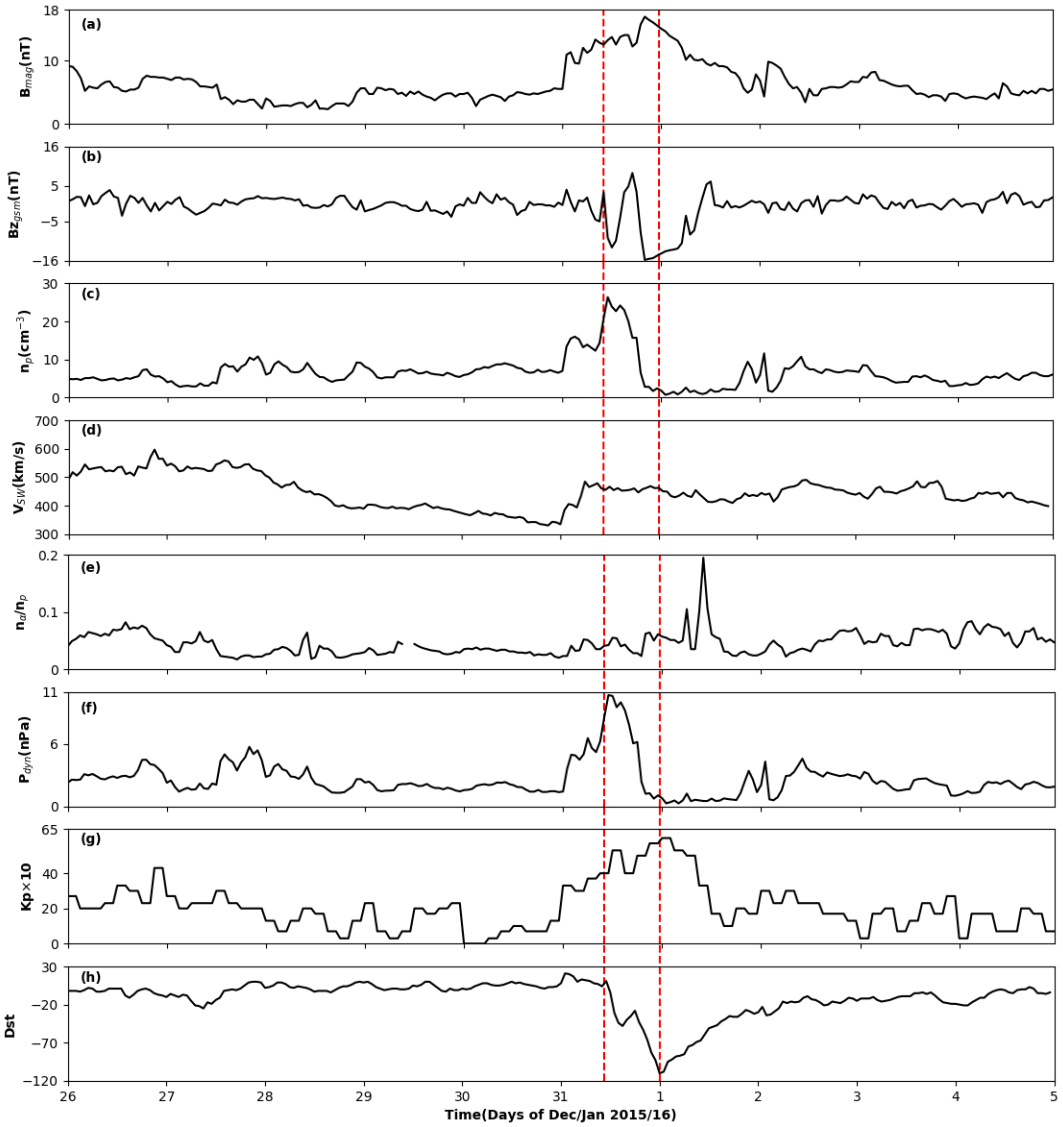

Figure 4.7: Geophysical and solar wind parameters of MC on 31 December 2015. The format is same as in Figure 4.1.

4.3.2 Particle dropouts

Figure 4.8 shows the observations of radiation belt particles fluxes by GOES-13 and GOES-15 satellites. Figure 4.8 (a) and (b) confirm that the flux dropout occurred

for the electron energy channels of $>$ 0.8 MeV and $>$ 2.0 MeV of both GOES-13 and GOES-15. The time of the flux dropout coincides with the MC. The temporal variation shows fluctuation at the time of MC onset as the magnetic field and increase after the MC, this is related to strongly enhanced substorm activities as shown in Figure 4.8. The net loss most-likely related to the magnetic disturbance resulted from the interaction of MC with magnetosphere. The protons temporal flux, $>$ 10 MeV, black curve, shows insignificant change. This also defer $>$ 30 MeV (Figure 4.8 (c)). This is not unexpected as dropout is energy dependant. Case 2 for instance shows large storm hence dropouts of $>$ 10 MeV while Case 1 did not show response from both $>$ 10 MeV and $>$ 30 MeV proton channels. The precipitation of proton is observed through all the cases under this investigation but not for lower energy protons. So, we again check POES precipitation for this event of broader interval as presented subsequently.

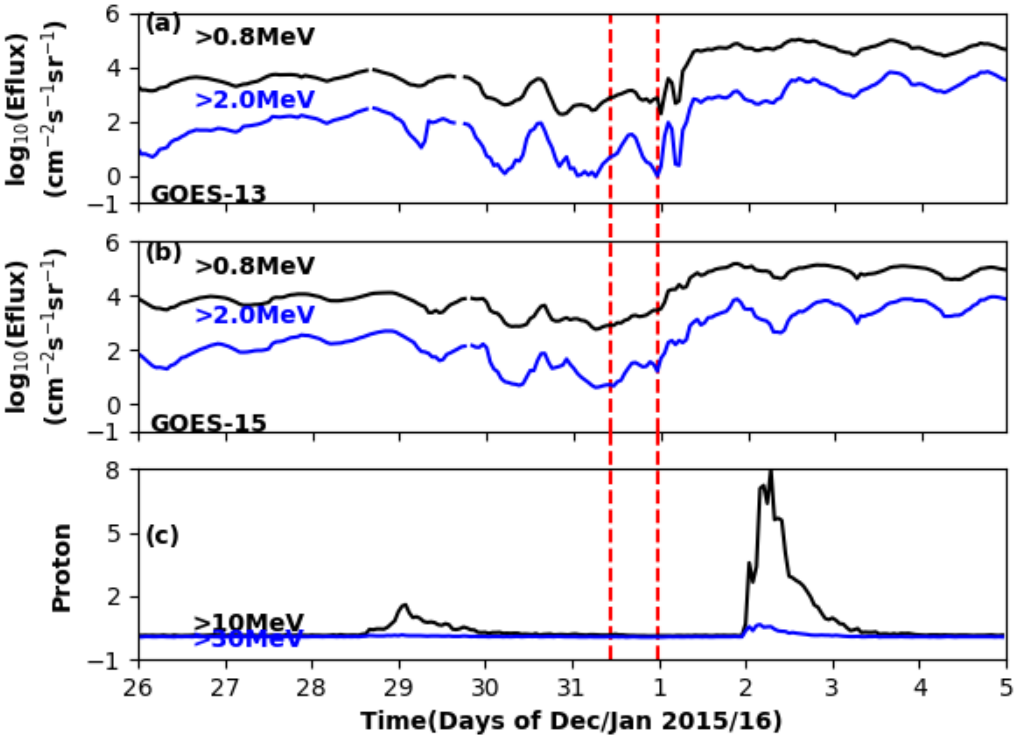

Figure 4.8: Particle flux measured by GOES satellites during MC-driven dropouts of 31 December 2015. The format is same as in Figure 4.2.

4.3.3 Particle precipitation

Figure 4.9 presents the MC triggered proton precipitation of ∽ 39 keV energy and electron precipitation of > 40 keV energy. Figure 4.9 (a), shows relatively small enhancement in proton precipitation which coincides to after the MC arrival which shows the small increase in proton flux which coincides to radiation belt particle dropouts. The precipitation of electron flux, however, is enhanced (Figure 4.9 (b)) this may lead to increase in energy absorption which may affect in the middle atmosphere.

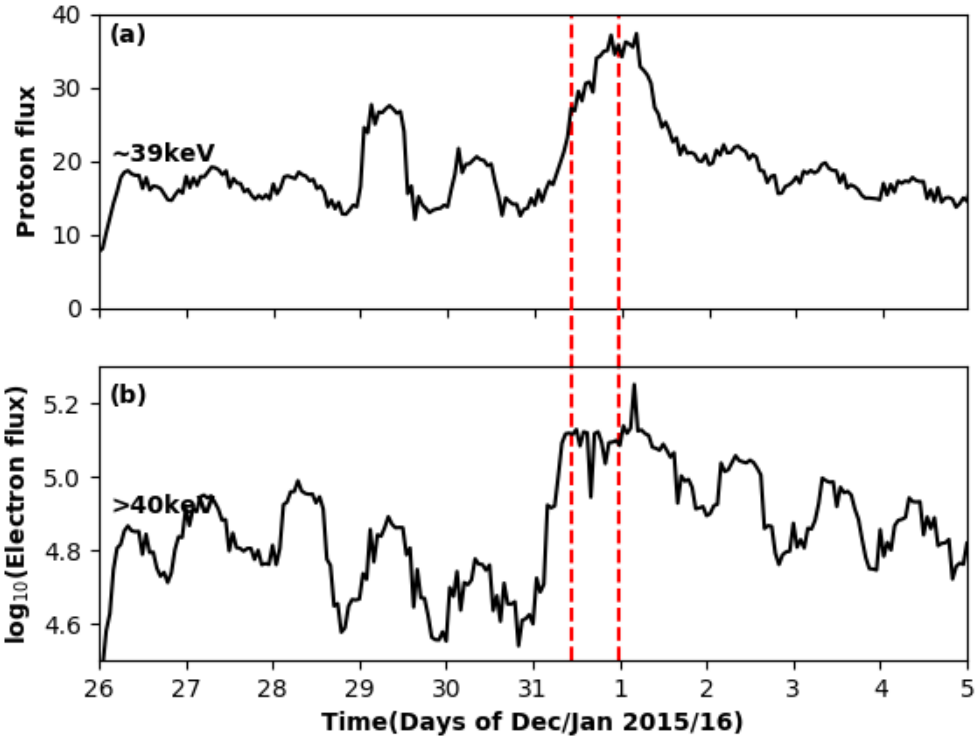

Figure 4.9: NOAA/POES particle precipitation on the arrival of MC. (a) ∽ 39 keV proton and (b) > 40 keV electron. The format is same as in Figure 4.3.

4.4 Case 4: MC event of 13 October 2016

4.4.1 Geophysical properties

We also check for most recent MC event. Figure 4.10 shows the geophysical parameters for MC that occurred on 13 October 2016. The IMF magnitude, again is enhanced to about 24 nT (Figure 4.10 (a)). The z-component of the IMF (Figure 4.10

(b)) went down to about -20 nT. This indicates strong outward radial diffusion. It means the magnetosphere is moved or pushed downward from its storm-off location. This is expected to cause the close magnetic field path to open and enhance or aid loss of particles in the drift loss cone (Blake et al., 2001). Also, the plasma number density deceased as observed in Figure 4.10 (c). Figure 4.10 (d) shows a small sudden increase of solar wind to above 440 km/s on 13 October MC arrival and further the speed intensified to above 700 km/s in later days. The solar wind dynamic pressure increases and for a while and decreases (Figure 4.10 (f)) as the storm passes. Similar to previous events, a high K_p index of +6 (Figure 4.10 (g)) as well as low D_{st} index of -104 nT (Figure 4.10 (h)) were observed which shows intensification of ring current.

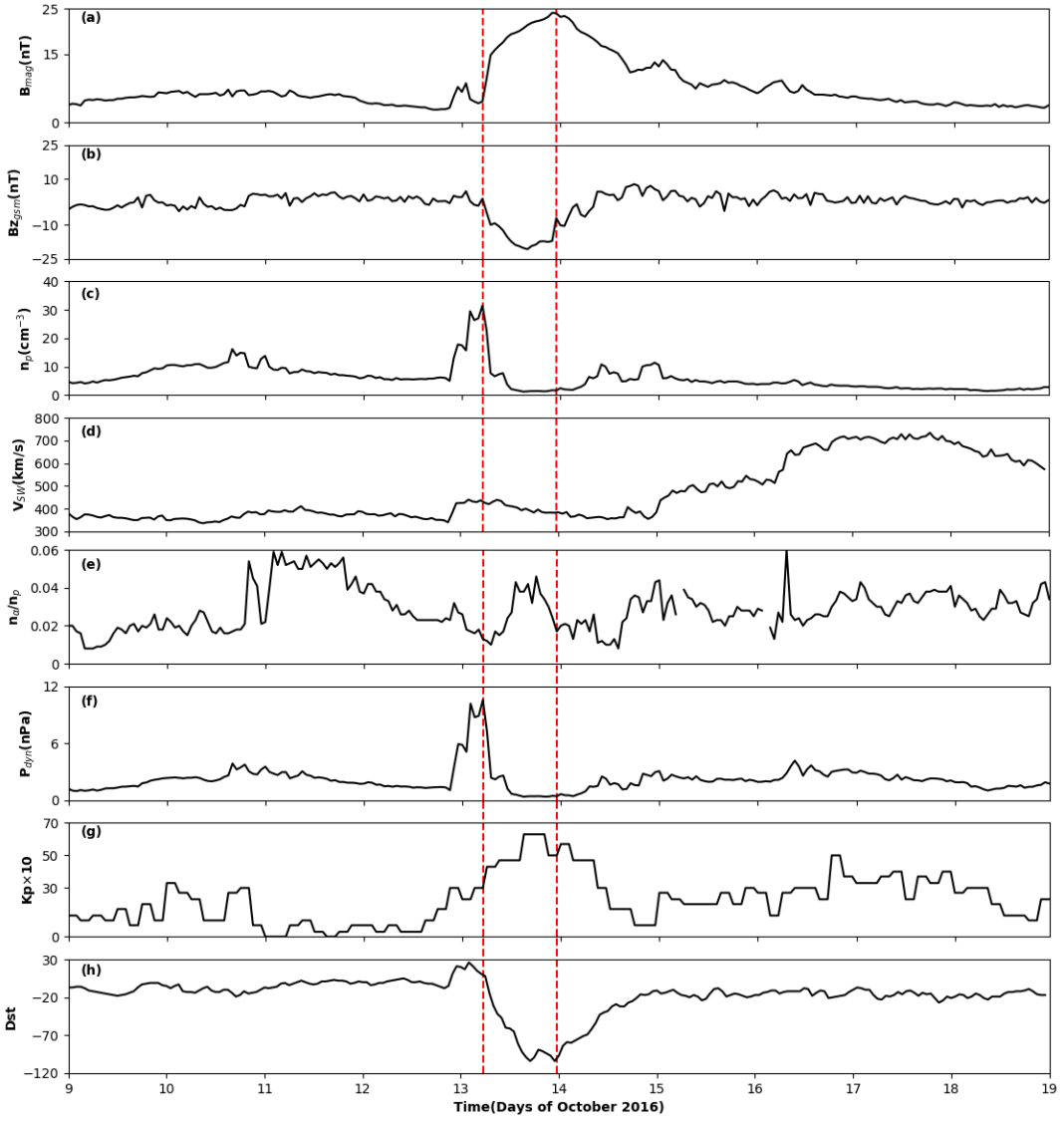

Figure 4.10: Geophysical and solar wind parameters of MC on 13 October 2016. Format is same as in Figure 4.1.

4.4.2 Particle dropouts

Figure 4.11 (a), (b) and (c) confirm that the flux dropout occurred for electron energy channels of $>$ 0.8 MeV and $>$ 2 MeV of GOES-13, GOES-14, and GOES-15. The time of the flux dropouts coincides with the MC onset. The temporal variation shows fluctuation in the time of MC and increase after the MC passed in later days as result of enhanced substorm activities. The net dropout most-likely related to the magnetic disturbance resulted from the interaction of MC with magnetosphere rather that adiabatic variations. The MC triggered storms could not act on both $>$ 10 MeV and $>$ 30 MeV as shown in Figure 4.11 (d).

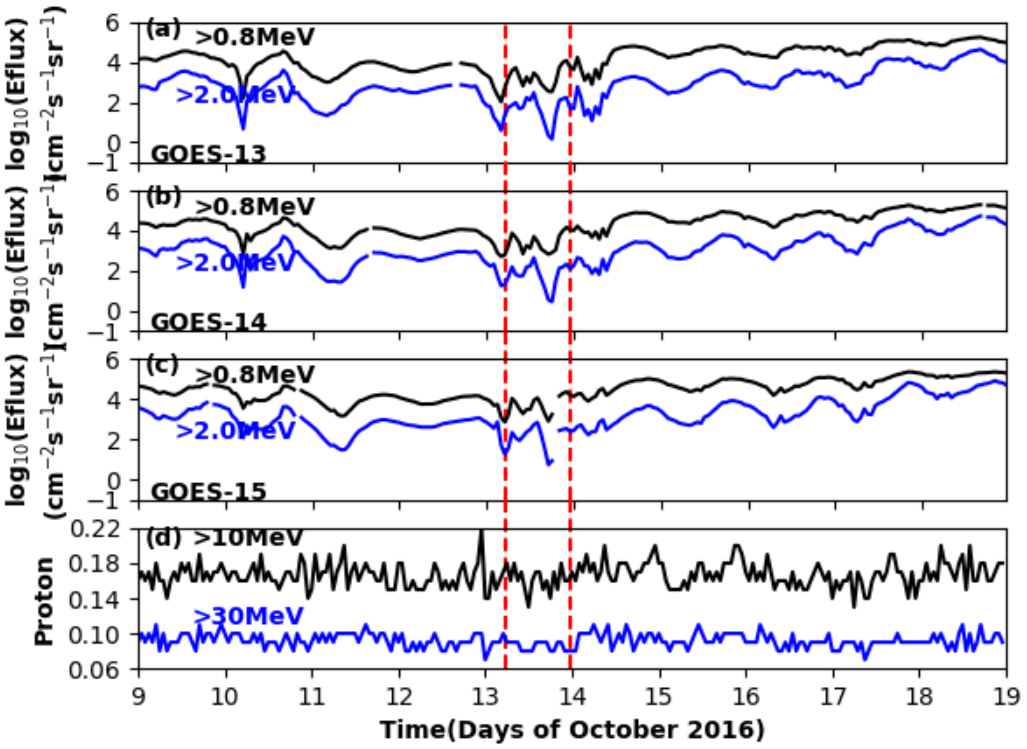

Figure 4.11: Particle flux measured by GOES satellites during MC-driven dropout of 13 October 2016. The format is same as in Figure 4.2.

4.4.3 Particle precipitation

Figure 4.12 presents the proton flux of energy $\backsim$ 39 keV and the electron flux of energy $>$ 40 keV. The proton shows peak (see Figure 4.12 (a)) after the MC arrival which shows the small increase in proton flux coincides to the MC onset and flux change

related to the radiation belt particle dropouts. The electron flux shows tendency for changes (Figure. 4.12 (b)) at the MC arrival.

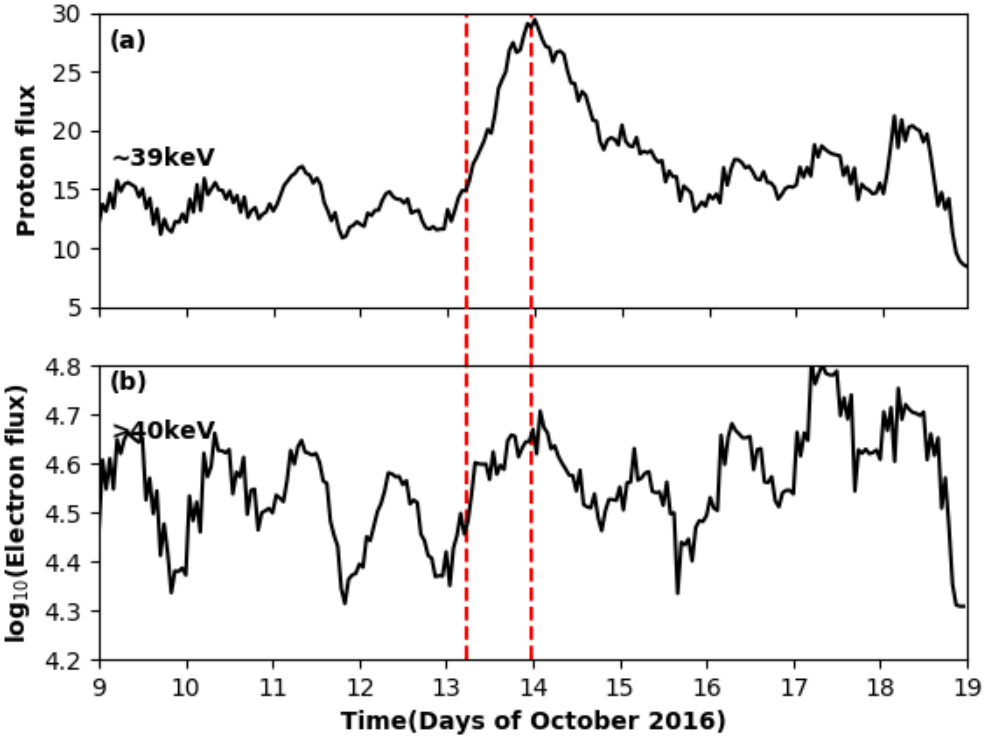

Figure 4.12: NOAA/POES particles precipitation on the arival of MC. (a) shows $\backsim$ 39 keV protons and (b) $>$ 40 keV electrons.

4.5 Summary and discussion

4.5.1 Summary

Case studies were presented for Geospace events on 29 April 2014, 17 March 2015, 31 December 2015 and 13 October 2016. For each Geospace event, the geophysical and solar wind conditions were analyzed to confirm MC-triggered storm. The analysis showed that the selected events exhibit properties of magnetic clouds and triggered geomagnetic storms. During each MC-triggered geomagnetic storm, radiation belt particles dropouts were observed. The dropouts of electron flux coincided with the enhancement of geomagnetic convection, intensification of ring current and other MC features such as intensification of interplanetary magnetic field and southward smooth rotation of its z-component. These sudden dropouts were caused by MC-driven geomagnetic storms and were in two order of magnitude on average in all energy channels

considered with subsequent recovery. The dropouts of proton strongly related to the severity of the storm. Insignificant dropouts were observed except for MC-even on 17 March 2015 in which a depletion of flux as observed. This particular event had caused large geomagnetic storm relative to other considered MC-driven geomagnetic storms events. POES satellites observations in LEO showed that some of the dropouts were indeed precipitated in to the atmosphere. The relative enhancement of particles in the lower energy channels confirm the precipitation. The enhancement coincides with arrival of MC and intensification of ring current.

4.5.2 Discussion

To study the effect of geomagnetic storms on the South African middle atmosphere MC events were selected. The MC events on 29 April 2014, 17 March 2015, 31 December 2015 and 13 October 2016 were examined for various geophysical properties. Each MC events were found to had triggered geomagnetic storms, hence enhanced magnetospheric convention. During the MC-triggered storms the radiation belt dropouts of electron flux began with an enhancement of interplanetary magnetospheric convection with K_p index increase and intensification of D_{st} index depression of geomagnetic disturbance observed from D_{st} index. The energetic particles dropouts from Van Allen radiation belt coincided with MC onset, which shows the radiation belt energetic electrons dropouts were caused by geomagnetic storms driven by MC. Significant electron dropouts were observed for both energy channels (> 0.8 MeV and > 0.8 MeV) in all events and were in 2 order of magnitude on average relative to prior and after event onset. Except for the first event (29 April 2014), the recovery exceeded the flux that was measured before the arrival of MC which maybe related to substorm activity influenced or other contributing phenomena. Proton dropouts were not significant for higher energies. However, MC on 17 March 2015 which is the largest geomagnetic storm event we consider in the current study shows dropout of proton > 10 MeV energy. Proton flux expected to show significant dropout during large geomagnetic storms or when there is a solar proton event. Large magnetic storms can act on higher proton energy and ultimately penetrate into the ionosphere.

So, the events on 17 March 2015 shows significant proton dropouts. For this particular date the proton flux, which was higher immediately before the arrival of MC, depleted completely during MC onset. There was a fluctuation of particles dropouts for some of the MC driven geomagnetic storms which coincided with the fluctuation of z-component of the magnetic field which shows the role of z-component of magnetic field.

Some of the particles dropouts from the radiation belt were seen to be precipitated into the South African middle atmosphere. Part of the dropouts might be due to Earth's magnetopause shadowing or through rapid outward radial transport (Turner et al., 2012). In most of the events the lower energy channels of both electron and proton which are expected to precipitate into and near the atmosphere of our region of interest (South African region) showed relative increase during MC. The relative increases that were observed found to be related to the elevation of K_p index, depression of D_{st} index due to intensification of ring current and smooth southwards rotation of z-component of the magnetic field.

One of the important responses of the middle atmosphere to geomagnetic storm is minor component composition, odd nitrogen and hydrogen, changes as a result of energetic particle impact on the the middle atmosphere which both contribute to ozone depletion in the atmosphere and related temperature variations (Laštovička, 1996). The coupling of chemical composition changes and propagation from the source region where composition change occurs can affect the dynamics of the atmosphere and atmospheric heating and cooling.

Chapter 5

Ionospheric response

5.1 Case 1: Event of 29 April 2014

5.1.1 Magnetometer measurements

Ground based magnetometer observations have played major role in the development of space weather by identifying ionospheric current in association with magnetic storms and substorms. As a result ground magnetometers observations are important measurements to study magnetosphere-ionosphere coupling. The South African magnetometer measurements data, Hermanus and Hartebeesthoek stations from SuperMag (*http://supermag.uib.no*), were employed to investigate the local magnetic field variations during the selected MC event to study ionospheric response. The hourly average of both the z-component and the total magnetic field were calculated from the one minute interval dataset of local ground magnetometer data obtained from the SuperMAG website.

Figure 5.1 presents hourly average of the total magnetic field and z-component of magnetic field at both Hermanus and Hartebeesthoek stations. The total magnetic field increased above 70 nT and the z-component depressed to below -25 nT at Hermanus (Figure 5.1 top panel). The peak was delayed for hours compared to the MC peak point for the disturbance caused by the MC takes time to reach the ground and inflict its effects. The Hartebeesthoek station result (Figure 5.1 bottom panel) shows similar pattern of magnetic field variation.

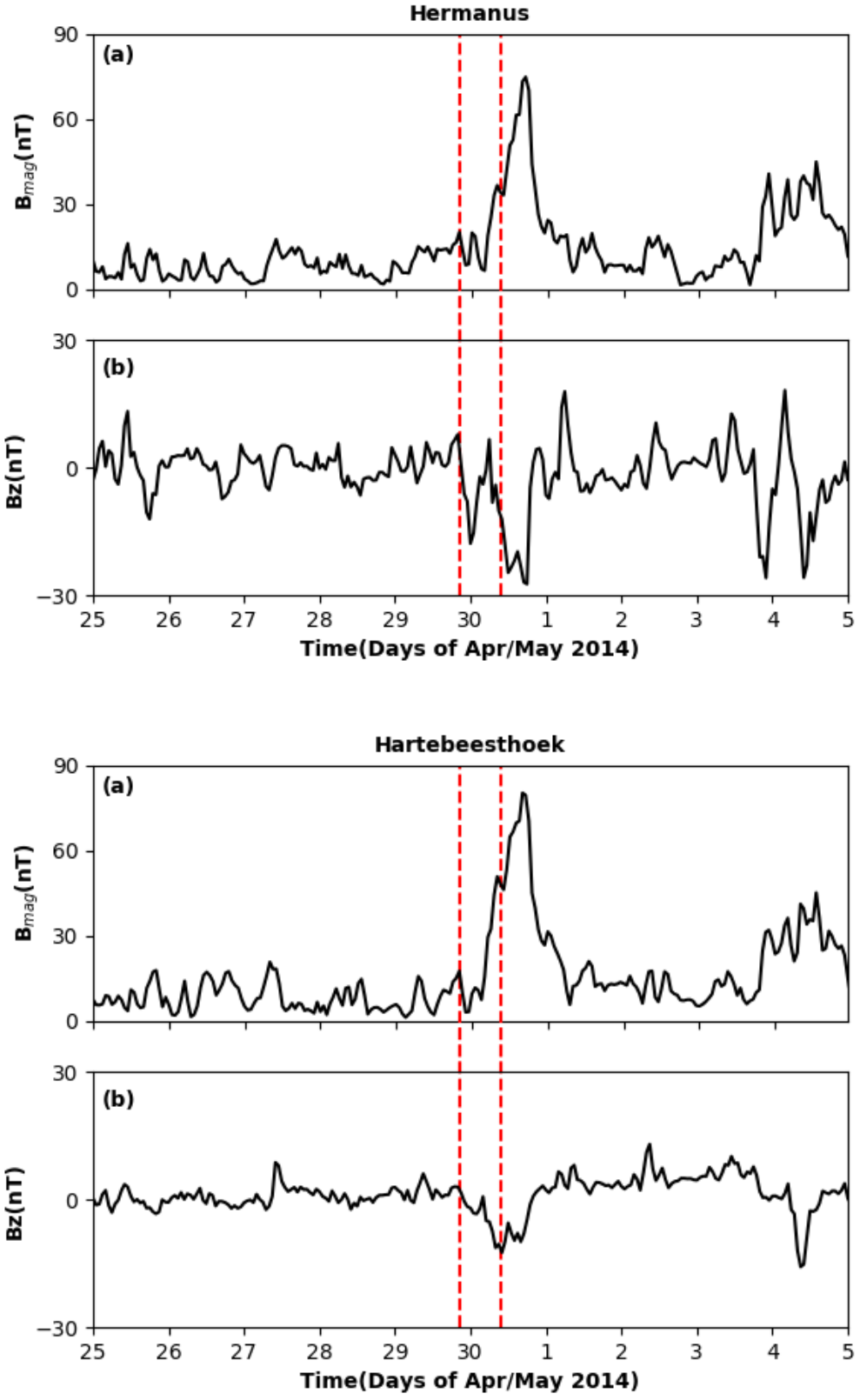

Figure 5.1: Magnetometer temporal variations on 29 April 2014 at Hermanus (top) and Hartebeesthoek (bottom). The vertical dotted lines indicate the MC interval as in Figure 4.1.

The magnetic field variation shows that the MC had intensified the ring current, which is a very important magnetosphere-ionosphere coupling reference, on this day the local ground magnetic field was significantly affected by MC, from which can be inferred that ionosphere also might have been affected with no exception to the middle atmosphere. During coronal mass ejection which is strongly related to MC, the response of low/mid-latitude ionosphere is large and mainly controlled by IMF B_z, which can be observed from ground magnetometer measurements, which determines how solar wind energy is transmitted into magnetosphere-ionosphere making ionospheric response distinctly linked to solar geomagnetic phenomenon (Rodríguez-Zuluaga et al., 2016). This disturbance of local magnetic field, which seen by enhancement of total ground magnetic field and depression of z-component of ground magnetic field due to MC, would allow precipitating particles energy to contribute to the energy capital of the middle atmosphere.

Ionosonde measures the ionosphere from the bottom and it is one of the very important observation to study the lower ionosphere. The lower ionosphere (h $<$ 100 km) is expected to enhance its electron concentration which results in altitude and critical frequency variations during intense geomagnetic storms. The geomagnetic storms cause a considerable increase of the pitch-angle diffusion, which forces the trapped energetic particles to move into the loss cone via wave-particle interactions and to precipitate into the ionosphere which the effect lasts for several days at mid-latitude (Danilov and Lastovicka, 2001). Nevertheless, the change in E-layer with respect to altitude and critical frequency were not available for this event. The following case study (Case 2) shows available ionospheric measurement.

5.2 Case 2: Event of 17 March 2015

5.2.1 Magnetometer measurements

Figure 5.2 presents hourly average of the total magnetic field and z-component of magnetic field at both Hermanus and Hartebeesthoek stations, the format is as in Figure 5.1. The total magnetic field increases well above 200 nT and the z-component depression reached -150 nT at Hermanus (Figure 5.2 top panel). The peak delayed for hours compared to the MC peak points for effect takes time to reach the ground. The Hartebeesthoek station result (Figure 5.2 bottom panel) shows similar trends of magnetic field variation. These are large magnetometer variation which are related MC.

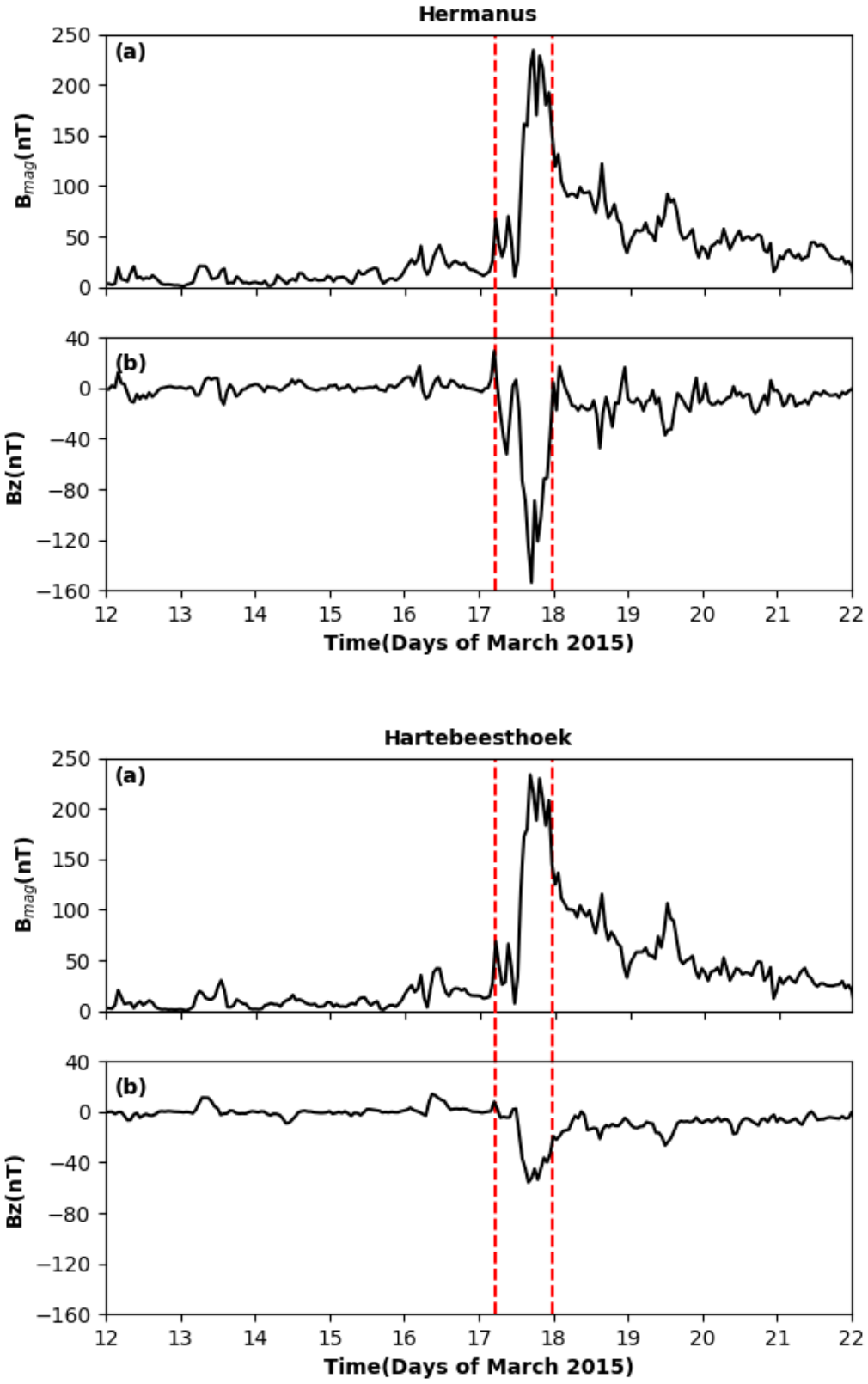

Figure 5.2: Magnetometer temporal variations on March 2017 at Hermanus (top) and Hartebeesthoek (bottom). The format is as in Figure 5.1.

It shows that this particular MC affected the local ground magnetometer from which can be inferred that ionosphere also might have been affected with no exception to the middle atmosphere. Again, this depression of magnetic field disturbance due to MC would allow the solar wind energy to contribute to the change of middle atmosphere.

5.2.2 Ionosonde measurements

As provided by the magnetometer measurement, any form of particle precipitation will result not only in the changes of ionospheric dynamics, but also its structure. Depending on the specific Geopsace event that triggers the storm, precipitation may be global or may only affect certain spatial region. To further correlate the precipitation with the ionospheric structure and dynamic over South Africa, we examined ionosondes measurements for any possible irregularities which may be associated with MC-triggered particle. It is generally expected that particles in the range of 30 eV - 30 keV, can essentially deposit most of their energies in the ionospheric E and F- layers. Therefore evidence of irregularities in ionisation density, provided by ionosonde, over South Africa ionosphere will indicate effects that could be attributed to MC-triggered precipitation. In this work we focused our attention on nighttime E-region ionisation variation. This is because daytime E-region is known to generally have high electron density values such that any extra ionisation and irregularities due to enhance precipitation may not be quickly recognized.

Figures 5.3, 5.4 and 5.5 show the ionosonde measurement from Hermanus, Grahamstown and Louisvale stations in South Africa respectively. The period of MC is indicated by the vertical dotted lines. Unfortunately most of the required critical nighttime E-layer frequencies were not available in the ionosonde measurements across all the stations considered. Note that the Grahamstown Nighttime E-region is characterised by low electron densities and high ion-electron collision frequencies. The gaps in the plots indicate non availability of data at that time. A quick look of ionosonde during other events earlier mentioned shows predominant data gaps hence will not be included. This makes it difficult to identify any irregularities that could be due to particle precipitation effects from ionosonde. Therefore it is almost impossible to draw any reasonable conclusions from the available ionosonde data. However, a closer look of the ground based magnetometer and the time history of the daytime E-layer critical frequency indicates that the E-region ionosphere was generally perturbed at MC arrival. As a consequence of the increase energy input into the ionosphere, frictional heating, which can then alter the lower thermospheric composition and neutral winds, can ensue, should the heating be impulsive, it can trigger travelling atmospheric disturbances (TADs). The TADs can propagate equatorward

by lifting the constant pressure surfaces (Roble, 1992), hence ionisation and enhanced conductivity (Ogunjobi et al., 2014). Due to the enhanced conductivity, currents can flow down to mid latitudes and even low latitudes as the magnetospheric convection causes the magnetopause to push inward (Foster et al., 1998 and Fejer and Emmert, 2003).

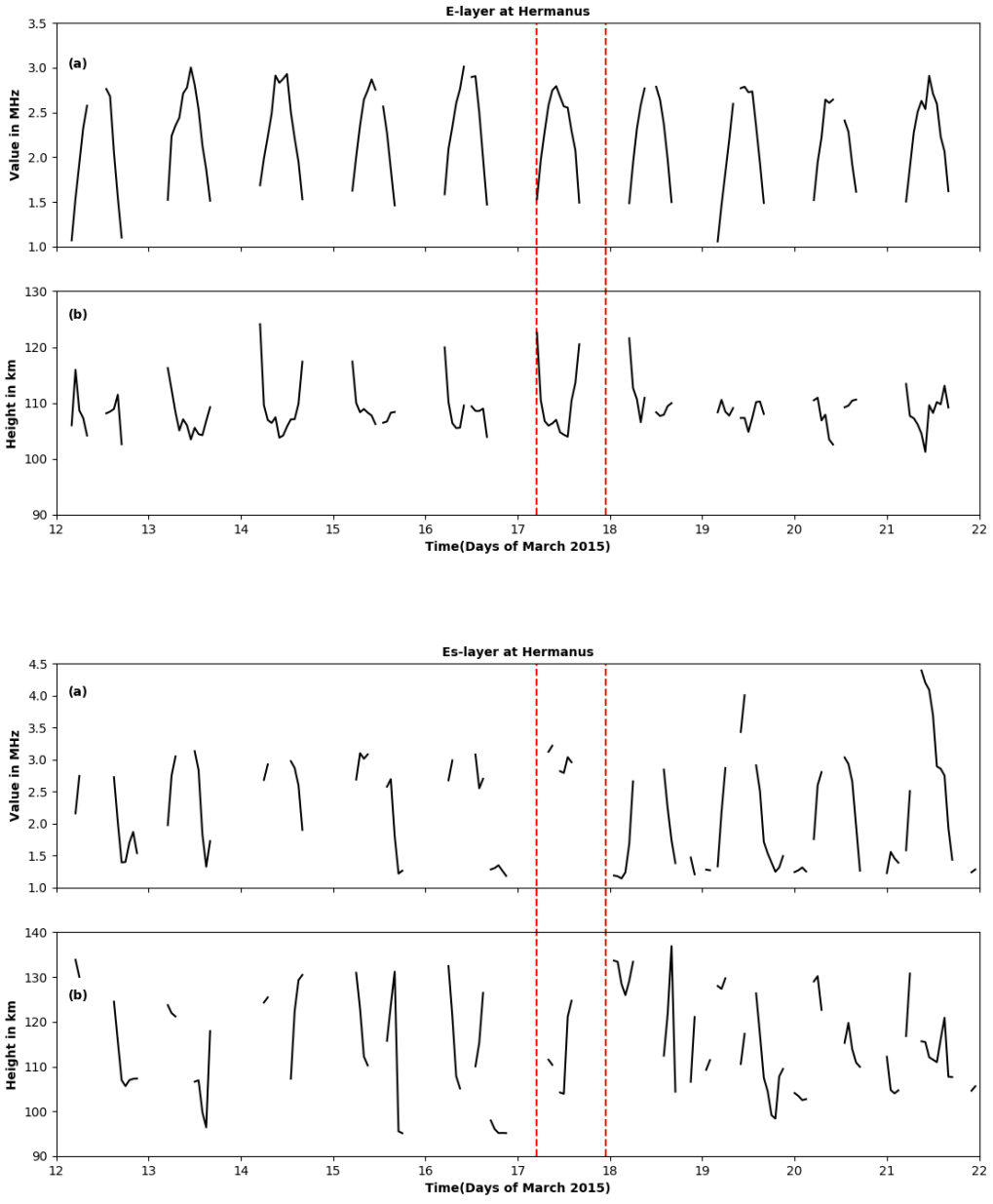

Figure 5.3: Ionosonde measurements at Heramanus. The E-layer critical frequency (a) and altitude (b)(Top panel), Es-layer (bottom panel). The vertical dotted lines indicate the MC interval as in Figure 4.1.

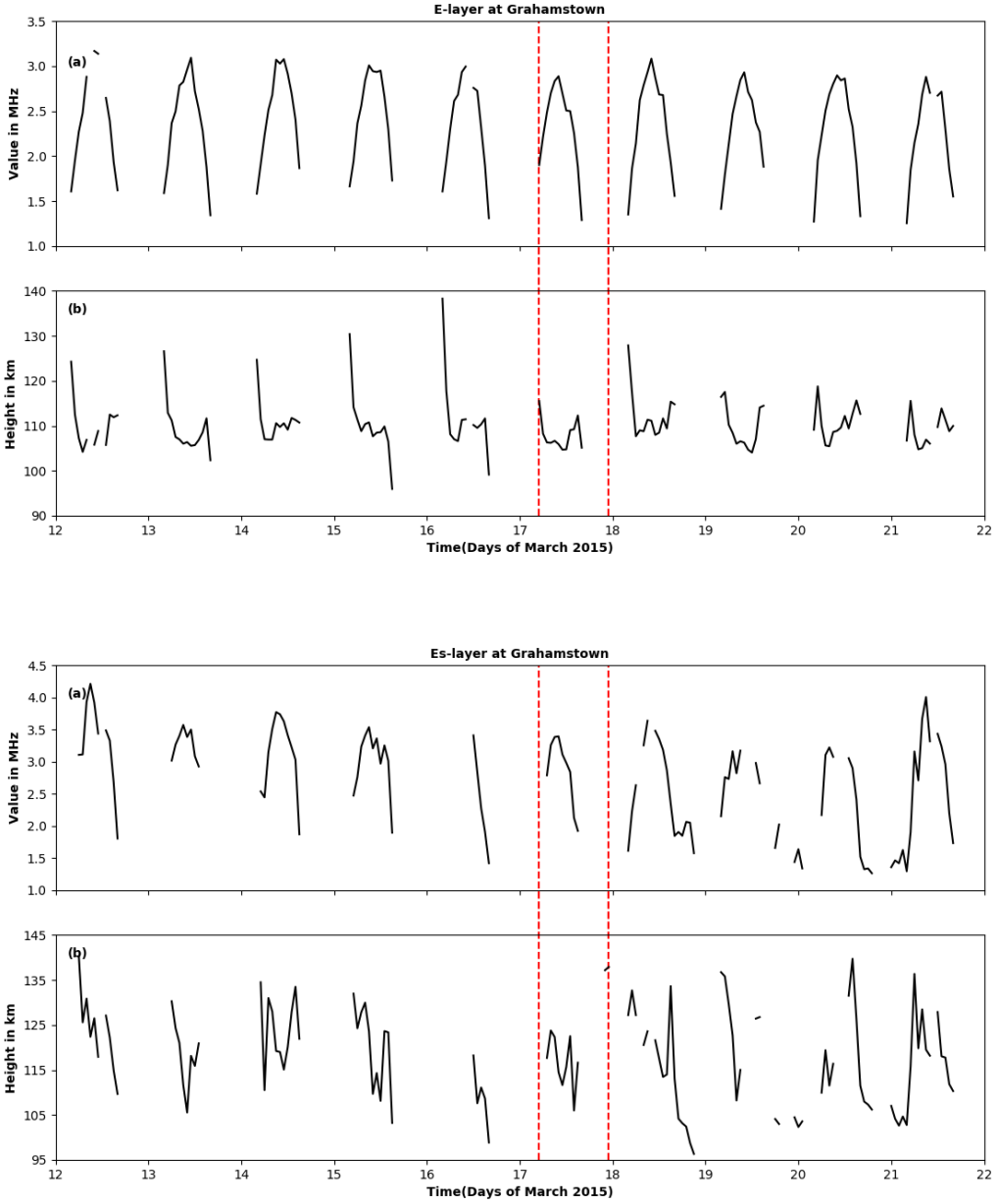

Figure 5.4: Ionosonde measurements at Grahamstown. The format is same as in Figure 5.3.

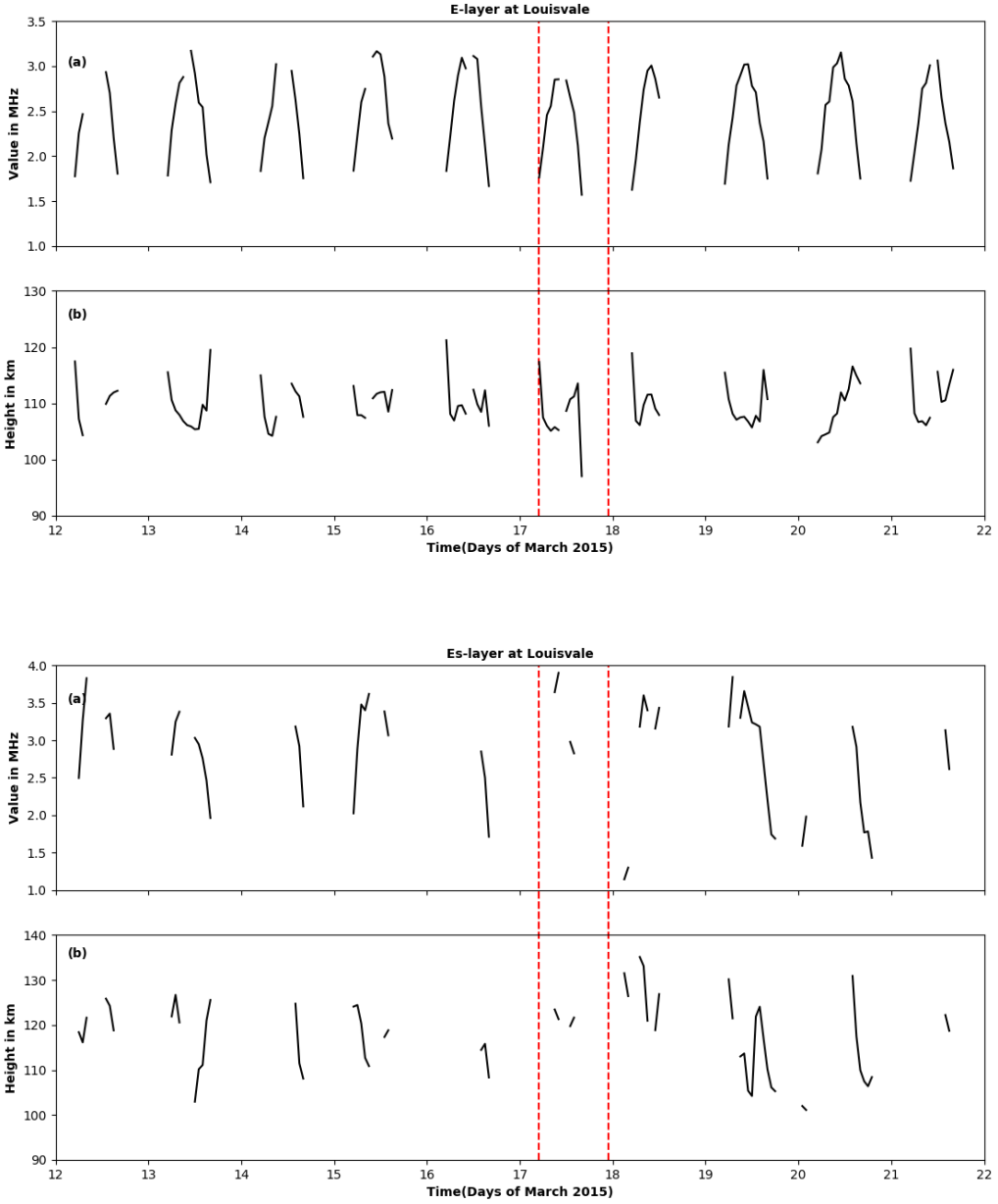

Figure 5.5: Ionosonde measurements at Louisvale. The format is same as in Figure 5.3.

5.3 Case 3: event of 31 December 2015

5.3.1 Magnetometer measurements

Figure 5.6 presents hourly average of the total magnetic field and z-component of magnetic field at both Hermanus and Hartebeesthoek stations, the format is as in Figure 5.1. The total magnetic field went well above 200 nT and the z-component depression reached -150 nT at Hermanus (Figure 5.6 top panel). The peak delayed for hours compared to the MC peak points for effect takes time to reach the ground. The Hartebeesthoek station result (Figure 5.6 bottom panel) shows similar pattern of magnetic field variation. These are high magnetometer variation which are related MC. It shows that this particular MC affected the local ground magnetometer from which can be inferred that ionosphere also might have been affected with no exception to the middle atmosphere. This depression of magnetic field disturbance due to MC would allow the solar wind energy to contribute to the change of middle atmosphere.

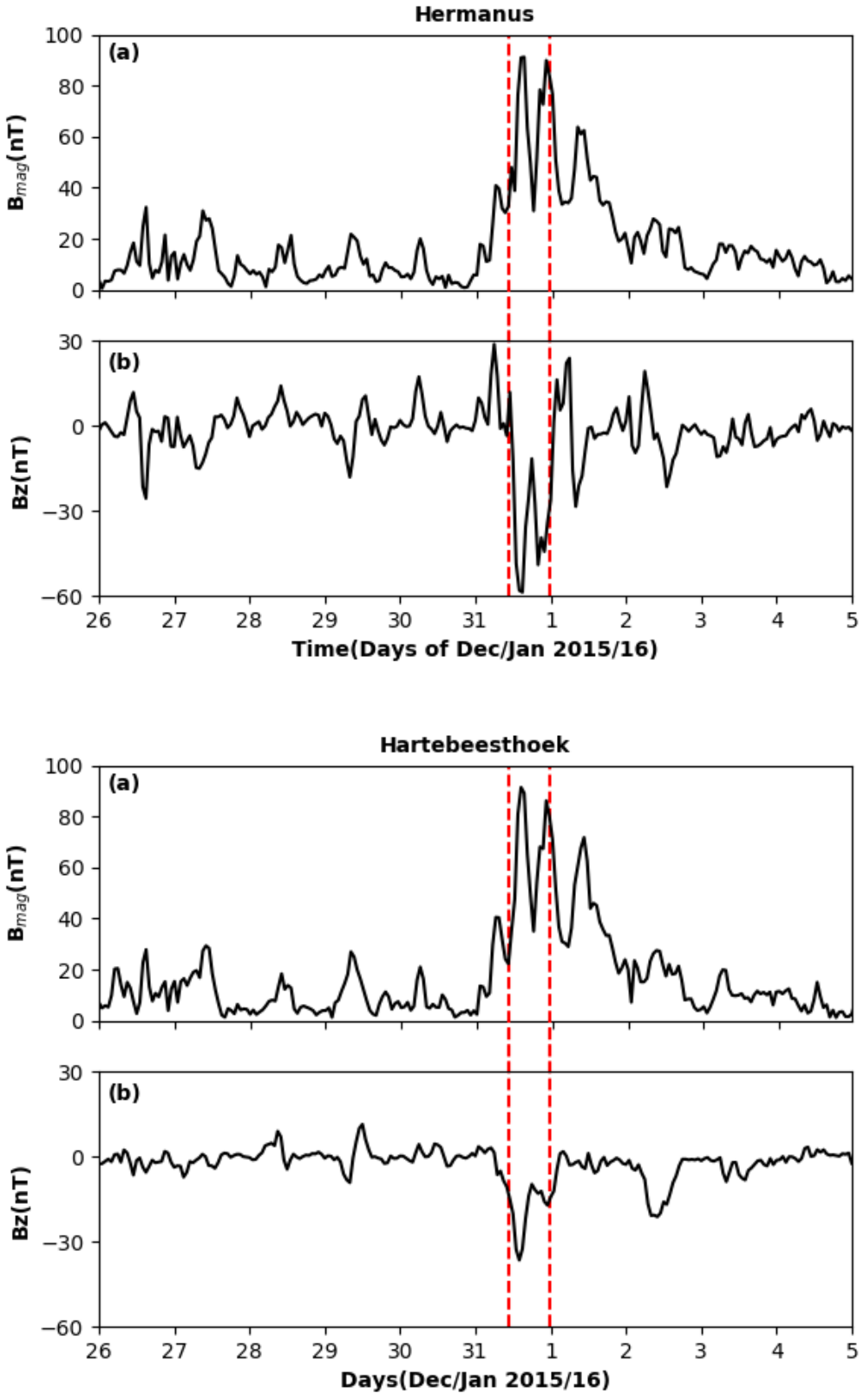

Figure 5.6: Magnetometer temporal variations at Hermanus(top) and Hartebeesthoek (bottom). The format is same as in Figure 5.1.

5.4 Case 4: Event of 13 October 2016

5.4.1 Magnetometer measurements

Figure 5.7 presents hourly average of the total magnetic field and z-component of magnetic field at both Hermanus and Hartebeesthoek stations, the format is as in Figure (5.1). The total magnetic field went well above 90 nT and the z-component depression reached about -60 nT at Hermanus (Figure 5.7 top panel (a) and (b) respectively). The Hartebeesthoek station result (Figure 5.7 bottom panel) shows similar pattern of magnetic field variation. These are big magnetometer variation which are related to MC compared to Case 1 and Case 3.

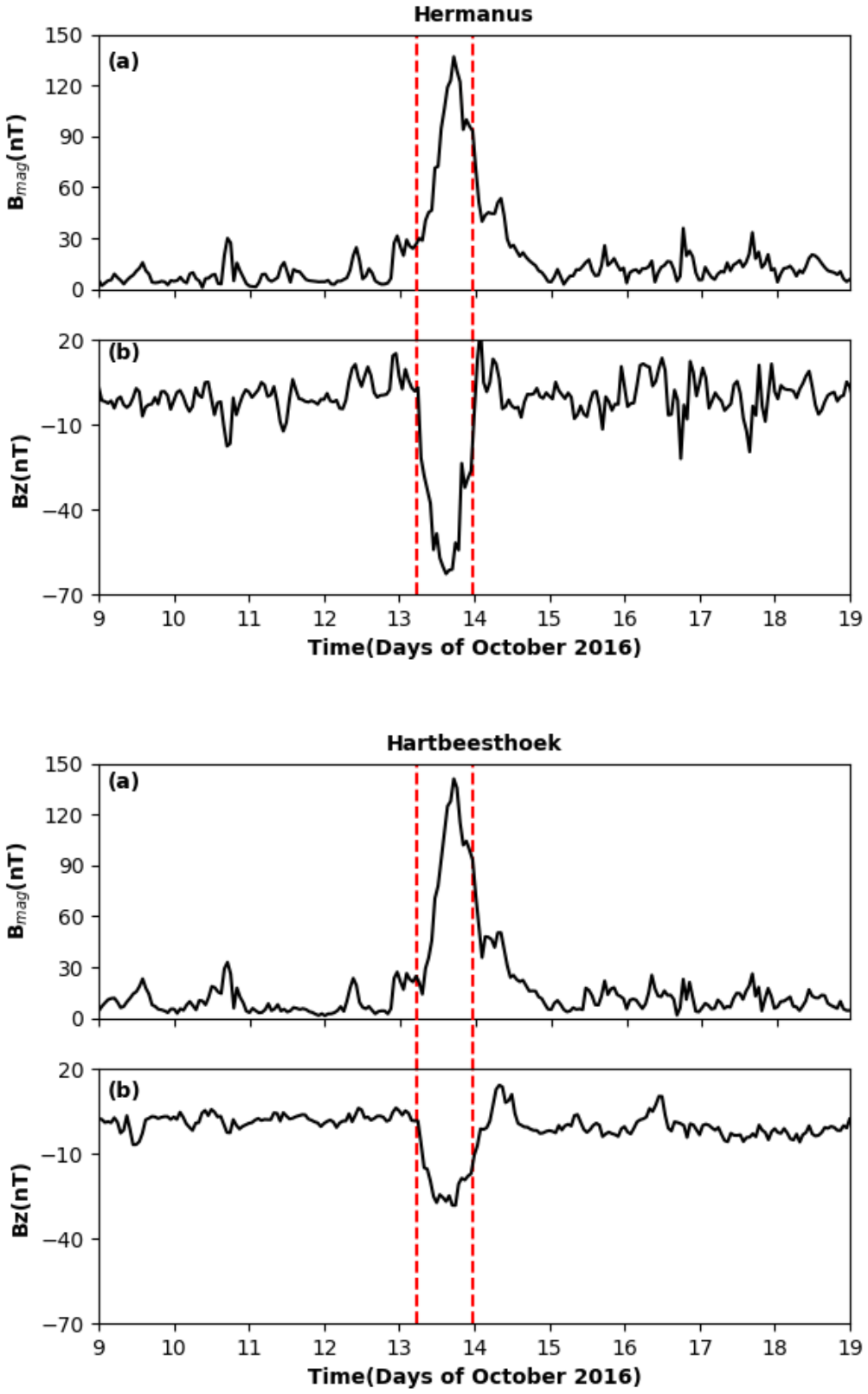

Figure 5.7: Magnetometer temporal variations at Hermanus (top) and Hartebeesthoek (bottom). The format is same as in Figure 5.1.

5.5 Summary and discussion

5.5.1 Summary

The South African ionospheric response is examined using local ionosonde data (Hermanus, Grahamston and Louisvale stations) and magnetometer data (Hermanus and Hartebeesthoek stations) for each event date. We expected E-layer altitude and critical frequency changes. However, the local ionosonde measurements were unavailable in majority of cases. However, there were strong indication of effect of geomagnetic disturbance locally observed from the two magnetometers in South Africa. The intensification of ring current that inferred from D_{st} index during MC is known to be important indicator of particles precipitation and related atmospheric effects, which indicates the local effect of geomagnetic storms triggered by MC.

5.5.2 Discussion

Particle precipitation is one of causal agent of changes in the atmosphere both in dynamics and compositions. As a result the upper ionosphere is continuously affected by the precipitation. The effect of precipitation is expected to noticeable in the layers the ionosphere. The magnetometer data obtained during the MC events under this study shows clear perturbation of the ionospheric structure. It is a well established fact that particles precipitations and related ionospheric effects enhanced at times when the ring current intensified which can be inferred from D_{st} index and when there is strong geomagnetic perturbation. During strong geomagnetic storms, the response of low/mid-latitude ionosphere is large and mainly controlled by IMF B_z, which can be observed from ground magnetometer measurements, determines how solar wind energy is transmitted into magnetosphere-ionosphere making ionospheric response distinctly linked to solar geomagnetic phenomenon (Rodríguez-Zuluaga et al., 2016). For all events, the localized magnetometer measurements show significant enhancements of the magnitude field magnitude and depression of z-component of the magnetic field. This shows that the MC events considered for this study had local effect and the geomagnetic storms might have been affected the middle atmosphere.

The geomagnetic storms cause a considerable increase of the pitch-angle diffusion, which forces the trapped energetic particles to move into the loss cone via wave-particle interactions and ultimately precipitate into the ionosphere. This effect can last for several days at mid-latitude (Danilov and Lastovicka, 2001). To further observe the local effect of geomagnetic storms caused by MC in the lower ionosphere, the local (South African) ionosonde were inspected. The lower ionosphere was expected

to have altitude change and critical frequency enhancement during MC events with a very less magnitude compared to the upper ionosphere. However, all local ionosonde observations showed huge data gap, making it almost impossible to draw any scientific conclusion.

Chapter 6

Summary and Future Direction

6.1 Summary

This study presented events based investigation of the effect of MC-driven geomagnetic storms on the middle atmosphere. The analysis showed that the selected events exhibit proprieties of magnetic clouds and triggered geomagnetic storms.

During each geomagnetic storm, GOES satellites data radiation belt particles dropouts were observed. The dropouts of electron flux coincided with the enhancement of geomagnetic convection, intensification of ring current and other MC features such as intensification of interplanetary magnetic field and southward smooth rotation of its z-component. These sudden dropouts were caused by MC-driven geomagnetic storms and were in two order of magnitude on average in all energy channels considered with subsequent recovery. The dropouts of protons strongly related to the severity of the storm. Insignificant dropouts were observed except for MC-even on 17 March 2015 in which a depletion of flux observed. This particular event had caused big geomagnetic storm comparing with other considered MC-driven geomagnetic storms events and it is the biggest geomagnetic storm in the current solar cycle so far.

POES satellites observations in LEO showed that some the dropouts were indeed participated in to the atmosphere. The relative enhancement of particles in the lower energy channels were confirm the precipitation. The enhancement coincides with arrival of MC and intensification of ring current which confirms the precipitation associated with geomagnetic storm triggered by MC. These precipitations are causal agents of energy balance that reflects in change of compositions and temperature in the atmosphere. However, the local ionosonde measurements (Hermanus, Grahamston and Louisvale) show no significant changes of E-layer altitude and plasma critical frequency variation.

The results also showed that there were strong geomagnetic disturbance locally observed from two magnetometers in South Africa (Hermanus and Hartebeesthoek). The intensification of ring current that inferred from D_{st} index during MC is known to be importation indicator of particles precipitation and related atmospheric effects, which indicates the local effect of geomagnetic storms triggered MC.

6.2 Future perspectives

The particle dropouts to the atmosphere can be further studied using other satellites data such as EPT/PROBA-V which has better distinctive particles measurements to compare with the present study. This study did not consider comparison of the responses to the upper atmosphere, future works may consider how the middle atmosphere geomagnetic storm-time response compared to the upper atmosphere using ionosonde data. The ground based local magnetometers responded with strong local geomagnetic disturbance which can be coupled with energetic particle precipitation. Also, the local ionosonde measurements did not show any significant change in E-layer. Hence, the middle atmosphere response during geomagnetic storm and its overall dynamics can not be completely described for the selected MC-driven geomagnetic storms. Future works are required to consider in this regards widening the number of events or select other type of Geospace event (particularly those in attendant of corotating interaction region) to confirm direct response in the lower ionosphere.

Bibliography

E. Antonucci, J. Hoeksema, and P. Scherrer. Rotation of the photospheric magnetic fields-a north-south asymmetry. *The Astrophysical Journal*, 360:296–304, 1990.

D. Baker. Coupling between the solar wind, magnetosphere, ionosphere and neutral atmosphere. *University of Colorado, Boulder, CO*, 80309, 2004.

D. Baker, S. Kanekal, V. Hoxie, M. Henderson, X. Li, H. E. Spence, S. Elkington, R. Friedel, J. Goldstein, M. Hudson, et al. A long-lived relativistic electron storage ring embedded in earths outer van allen belt. *Science*, 340(6129):186–190, 2013.

G. Bazilevskaya, I. Usoskin, E. Flückiger, R. Harrison, L. Desorgher, R. Bütikofer, M. Krainev, V. Makhmutov, Y. I. Stozhkov, A. Svirzhevskaya, et al. Cosmic ray induced ion production in the atmosphere. *Space Science Reviews*, 137(1-4):149–173, 2008.

J. Blake, U. Inan, M. Walt, T. Bell, J. Bortnik, D. Chenette, and H. Christian. Lightning-induced energetic electron flux enhancements in the drift loss cone. *Journal of Geophysical Research*, 106(A12):29733–29744, 2001.

V. Bothmer and I. A. Daglis. *Space weather: physics and effects*. Springer Science & Business Media, 2007.

L. Burlaga. Multifractal structure of the interplanetary magnetic field: Voyager 2 observations near 25 au, 1987-1988. *Geophysical Research Letters*, 18(1):69–72, 1991.

L. Burlaga, E. Sittler, F. Mariani, and R. Schwenn. Magnetic loop behind an interplanetary shock: Voyager, helios, and imp 8 observations. *Journal of Geophysical Research*, 86(A8):6673–6684, 1981.

L. Burlaga, L. Klein, N. Sheeley, D. Michels, R. Howard, M. Koomen, R. Schwenn, and H. Rosenbauer. A magnetic cloud and a coronal mass ejection. *Geophysical Research Letters*, 9(12):1317–1320, 1982.

L. Burlaga, R. Fitzenreiter, R. Lepping, K. Ogilvie, A. Szabo, A. Lazarus, J. Steinberg, G. Gloeckler, R. Howard, D. Michels, et al. A magnetic cloud containing prominence material: January 1997. *Journal of Geophysical Research*, 103(A1): 277–285, 1998.

L. Burlaga, S. Plunkett, and O. St Cyr. Successive cmes and complex ejecta. *Journal of Geophysical Research*, 107(A10), 2002.

W. H. Campbell. Geomagnetic storms, the dst ring-current myth and lognormal distributions. *Journal of Atmospheric and Terrestrial Physics*, 58(10):1171–1187, 1996.

F. F. Chen and S. E. von Goeler. Introduction to plasma physics and controlled fusion volume 1: Plasma physics. *Physics Today*, 38:87, 1985.

J. Chen and D. A. Garren. Interplanetary magnetic clouds: Topology and driving mechanism. *Geophysical research letters*, 20(21):2319–2322, 1993.

M. A. Clilverd, R. Duthie, R. Hardman, A. T. Hendry, C. J. Rodger, T. Raita, M. Engebretson, M. R. Lessard, D. Danskin, and D. K. Milling. Electron precipitation from emic waves: A case study from 31 may 2013. *Journal of Geophysical Research*, 120(5):3618–3631, 2015.

A. Danilov and J. Lastovicka. Effects of geomagnetic storms on the ionosphere and atmosphere. *International Journal of Geomagnetism and Aeronomy*, 2(3):209–224, 2001.

K. Davies. *Ionospheric radio*. Number 31. IET, 1990.

C. R. DeVore. Magnetic helicity generation by solar differential rotation. *The Astrophysical Journal*, 539(2):944, 2000.

J. W. Dungey. Interplanetary magnetic field and the auroral zones. *Physical Review Letters*, 6(2):47, 1961.

D. S. Evans and M. S. Greer. *Polar Orbiting Environmental Satellite Space Environment Monitor-2: Instrument Description and Archive Data Documentation*. US Department of Commerce, National Oceanic and Atmospheric Administration, Oceanic and Atmospheric Research Laboratories, Space Environment Center, 2000.

C. Farrugia, L. Burlaga, and R. Lepping. Magnetic clouds and the quiet-storm effect at earth. *Magnetic storms*, pages 91–106, 1997.

B. G. Fejer and J. Emmert. Low-latitude ionospheric disturbance electric field effects during the recovery phase of the 19–21 october 1998 magnetic storm. *Journal of Geophysical Research*, 108(A12), 2003.

J. Foster, S. Cummer, and U. S. Inan. Midlatitude particle and electric field effects at the onset of the november 1993 geomagnetic storm. *Journal of Geophysical Research*, 103(A11):26359–26366, 1998.

K. Georgieva, V. Tsanev, and B. Kirov. Solar asymmetry, qbo and climate. *Proceedings of the SPARC*, 2000.

K. Georgieva, B. Kirov, D. Atanassov, and A. Boneva. Impact of magnetic clouds on the middle atmosphere and geomagnetic disturbances. *Journal of atmospheric and solar-terrestrial physics*, 67(1):163–176, 2005.

J. Gjerloev. The supermag data processing technique. *Journal of Geophysical Research*, 117(A9), 2012.

H. Goldstein. On the field configuration in magnetic clouds, is solar wind five. *NASA Conf. Publ. 2280, pp.731*, 1983.

W. Gonzalez, J. Joselyn, Y. Kamide, H. Kroehl, G. Rostoker, B. Tsurutani, and V. Vasyliunas. What is a geomagnetic storm? *Journal of Geophysical Research*, 99(A4):5771–5792, 1994.

W. D. Gonzalez and B. T. Tsurutani. Criteria of interplanetary parameters causing intense magnetic storms (d st¡- 100 nt). *Planetary and Space Science*, 35(9):1101–1109, 1987.

J. Green, T. Onsager, T. O'Brien, and D. Baker. Testing loss mechanisms capable of rapidly depleting relativistic electron flux in the earth's outer radiation belt. *Journal of Geophysical Research*, 109(A12), 2004.

J. C. Green and M. Kivelson. Relativistic electrons in the outer radiation belt: Differentiating between acceleration mechanisms. *Journal of Geophysical Research*, 109(A3), 2004.

J. R. Herman and R. A. Goldberg. Initiation of non-tropical thunderstorms by solar activity. *Journal of Atmospheric and Terrestrial Physics*, 40(2):121–134, 1978.

M. Hidalgo, C. Cid, A. Vinas, and J. Sequeiros. A non-force-free approach to the topology of magnetic clouds in the solar wind. *Journal of Geophysical Research*, 107(A1), 2002.

A. Hundhausen. Coronal mass ejections. In *The Many Faces of the Sun*, pages 143–200. Springer, 1999.

K. Huttunen, R. Schwenn, V. Bothmer, and H. Koskinen. Properties and geoeffectiveness of magnetic clouds in the rising, maximum and early declining phases of solar cycle 23. In *Annales Geophysicae*, volume 23, pages 625–641, 2005.

A. S. Jursa et al. *Handbook of geophysics and the space environment*. NTIS Springfield, VA, 1985.

S. Kahler. Coronal mass ejections. *Reviews of Geophysics*, 25(3):663–675, 1987.

M. Kelley. The earth's ionosphere: Plasma physics and electrodynamics, ser. *International Geophysics*, 43, 2009.

J. King and N. Papitashvili. Solar wind spatial scales in and comparisons of hourly wind and ace plasma and magnetic field data. *Journal of Geophysical Research*, 110(A2), 2005.

M. G. Kivelson and C. T. Russell. *Introduction to space physics*. Cambridge university press, 1995.

K. Labitzke and H. V. Loon. Association between the 11-yr solar cycle, the qbo, and the atmosphere. part iii: Aspects of the association. *Journal of Climate*, 2(6): 554–565, 1989.

M. M. Lam, R. B. Horne, N. P. Meredith, S. A. Glauert, T. Moffat-Griffin, and J. C. Green. Origin of energetic electron precipitation¿ 30 kev into the atmosphere. *Journal of Geophysical Research*, 115(A4), 2010.

J. Laštovička. Effects of geomagnetic storms in the lower ionosphere, middle atmosphere and troposphere. *Journal of Atmospheric and Terrestrial Physics*, 58(7): 831–843, 1996.

R. Lepping, L. Burlaga, A. Szabo, K. Ogilvie, W. Mish, D. Vassiliadis, A. Lazarus, J. Steinberg, C. Farrugia, L. Janoo, et al. The wind magnetic cloud and events of october 18–20, 1995: Interplanetary properties and as triggers for geomagnetic activity. *Journal of Geophysical Research*, 102(A7):14049–14063, 1997.

K. Marubashi. Structure of the interplanetary magnetic clouds and their solar origins. *Advances in Space Research*, 6(6):335–338, 1986.

K. May-Britt. Space physics: an introduction to plasmas and particles in the heliosphere and magnetospheres, 2001.

C. E. McIlwain. Magnetic coordinates. In *Radiation Trapped in the Earth's Magnetic Field*, pages 45–61. Springer, 1966.

R. T. Merrill and M. W. McElhinny. *The Earth's magnetic field: Its history, origin and planetary perspective*, volume 401. Academic Press London, 1983.

R. Millan and R. Thorne. Review of radiation belt relativistic electron losses. *Journal of Atmospheric and Solar-Terrestrial Physics*, 69(3):362–377, 2007.

I. A. Mironova, K. L. Aplin, F. Arnold, G. A. Bazilevskaya, R. G. Harrison, A. A. Krivolutsky, K. A. Nicoll, E. V. Rozanov, E. Turunen, and I. G. Usoskin. Energetic particle influence on the earth's atmosphere. *Space Science Reviews*, 194(1-4):1–96, 2015.

P. Morrison. Solar-connected variations of the cosmic rays. In *Physical Review*, volume 95, pages 646–646. AMERICAN PHYSICAL SOC ONE PHYSICS ELLIPSE, COLLEGE PK, MD 20740-3844 USA, 1954.

O. Ogunjobi, V. Sivakumar, and N. Mbatha. A case study of energy deposition and absorption by magnetic cloud electrons and protons over the high latitude stations: Effects on the mesosphere and lower thermosphere. *Terrestrial, Atmospheric & Oceanic Sciences*, 25(2), 2014.

T. Onsager, R. Grubb, J. Kunches, L. Matheson, D. Speich, R. W. Zwickl, and H. Sauer. Operational uses of the goes energetic particle detectors. In *SPIE's 1996 International Symposium on Optical Science, Engineering, and Instrumentation*, pages 281–290. International Society for Optics and Photonics, 1996.

T. Onsager, G. Rostoker, H.-J. Kim, G. Reeves, T. Obara, H. Singer, and C. Smithtro. Radiation belt electron flux dropouts: Local time, radial, and particle-energy dependence. *Journal of Geophysical Research*, 107(A11), 2002.

E. Parker. Dynamical theory of the solar wind. *Space Science Reviews*, 4(5-6):666–708, 1965.

V. Pierrard and G. Lopez Rosson. The effects of the big storm events in the first half of 2015 on the radiation belts observed by ept/proba-v. *Annales Geophysicae (09927689)*, 34(1), 2016.

E. Priest. The sun and its magnetohydrodynamics. *Introduction to space physics*, pages 58–90, 1995.

C. Randall, V. Harvey, C. Singleton, S. Bailey, P. Bernath, M. Codrescu, H. Nakajima, and J. Russell. Energetic particle precipitation effects on the southern hemisphere stratosphere in 1992–2005. *Journal of Geophysical Research*, 112(D8), 2007.

J. A. Ratcliffe. Introduction to the ionosphere and magnetosphere. 1972.

G. Reeves, K. McAdams, R. Friedel, and T. O'Brien. Acceleration and loss of relativistic electrons during geomagnetic storms. *Geophysical Research Letters*, 30(10), 2003.

I. Richardson and H. Cane. Near-earth interplanetary coronal mass ejections during solar cycle 23 (1996–2009): Catalog and summary of properties. *Solar Physics*, 264 (1):189–237, 2010.

R. Roble. The polar lower thermosphere. *Planetary and space science*, 40(2-3):271–297, 1992.

C. J. Rodger, M. A. Clilverd, J. C. Green, and M. M. Lam. Use of poes sem-2 observations to examine radiation belt dynamics and energetic electron precipitation into the atmosphere. *Journal of Geophysical Research*, 115(A4), 2010.

J. Rodríguez-Zuluaga, S. Radicella, B. Nava, C. Amory-Mazaudier, H. Mora-Páez, and K. Alazo-Cuartas. Distinct responses of the low-latitude ionosphere to cme and hssws: The role of the imf bz oscillation frequency. *Journal of Geophysical Research*, 121(11), 2016.

E. C. Roelof and D. G. Sibeck. Magnetopause shape as a bivariate function of interplanetary magnetic field bz and solar wind dynamic pressure. *Journal of Geophysical Research*, 98(A12):21421–21450, 1993.

T. Rosenberg, L. Lanzerotti, C. Maclennan, and C. Evans. Impulsive, quasi-periodic variations in ionospheric absorption of cosmic radio noise. *Journal of geomagnetism and geoelectricity*, 31(6):585–597, 1979.

D. Rusch, J.-C. Gerard, S. Solomon, P. Crutzen, and G. Reid. The effect of particle precipitation events on the neutral and ion chemistry of the middle atmospherei. odd nitrogen. *Planetary and Space Science*, 29(7):767–774, 1981.

A. Seppälä, P. Verronen, E. Kyrölä, S. Hassinen, L. Backman, A. Hauchecorne, J. Bertaux, and D. Fussen. Solar proton events of october–november 2003: Ozone depletion in the northern hemisphere polar winter as seen by gomos/envisat. *Geophysical research letters*, 31(19), 2004.

M. Sinnhuber, H. Nieder, and N. Wieters. Energetic particle precipitation and the chemistry of the mesosphere/lower thermosphere. *Surveys in Geophysics*, 33(6): 1281–1334, 2012.

S. Solomon, P. J. Crutzen, and R. G. Roble. Photochemical coupling between the thermosphere and the lower atmosphere: 1. odd nitrogen from 50 to 120 km. *Journal of Geophysical Research: Oceans*, 87(C9):7206–7220, 1982.

F. Søraas, M. I. Sandanger, and C. Smith-Johnsen. Noaa poes and metop particle observations during the 17 march 2013 storm. *Journal of Atmospheric and Solar-Terrestrial Physics*, 2017.

R. M. Thorne. The importance of energetic particle precipitation on the chemical composition of the middle atmosphere. *pure and applied geophysics*, 118(1):128–151, 1980.

R. M. Thorne. Radiation belt dynamics: The importance of wave-particle interactions. *Geophysical Research Letters*, 37(22), 2010.

B. Tsurutani and W. Gonzalez. The future of geomagnetic storm predictions: implications from recent solar and interplanetary observations. *Journal of Atmospheric and Terrestrial Physics*, 57(12):1369–1384, 1995.

B. T. Tsurutani, W. D. Gonzalez, F. Tang, S. I. Akasofu, and E. J. Smith. Origin of interplanetary southward magnetic fields responsible for major magnetic storms near solar maximum (1978–1979). *Journal of Geophysical Research*, 93(A8):8519–8531, 1988.

D. Turner, V. Angelopoulos, W. Li, J. Bortnik, B. Ni, Q. Ma, R. Thorne, S. Morley, M. Henderson, G. Reeves, et al. Competing source and loss mechanisms due to wave-particle interactions in earth's outer radiation belt during the 30 september to 3 october 2012 geomagnetic storm. *Journal of Geophysical Research*, 119(3): 1960–1979, 2014.

D. L. Turner, Y. Shprits, M. Hartinger, and V. Angelopoulos. Explaining sudden losses of outer radiation belt electrons during geomagnetic storms. *Nature Physics*, 8(3):208–212, 2012.

E. Turunen, P. T. Verronen, A. Seppälä, C. J. Rodger, M. A. Clilverd, J. Tamminen, C.-F. Enell, and T. Ulich. Impact of different energies of precipitating particles on nox generation in the middle and upper atmosphere during geomagnetic storms. *Journal of Atmospheric and Solar-Terrestrial Physics*, 71(10):1176–1189, 2009.

A. Vampola and D. Gorney. Electron energy deposition in the middle atmosphere. *Journal of Geophysical Research*, 88(A8):6267–6274, 1983.

J. A. Van Allen and L. A. Frank. Radiation around the earth to a radial distance of 107,400 km. *Nature*, 183(4659):430–434, 1959.

A. Varotsou, R. H. Friedel, G. D. Reeves, B. Lavraud, R. M. Skoug, T. E. Cayton, and S. Bourdarie. Characterization of relativistic electron flux rise times during the recovery phase of geomagnetic storms as measured by the ns41 gps satellite. *Journal of Atmospheric and Solar-Terrestrial Physics*, 70(14):1745–1759, 2008.

Y. M. Wang, P. Z. Ye, and S. Wang. Multiple magnetic clouds: Several examples during march–april 2001. *Journal of Geophysical Research*, 108(A10), 2003.

D. Weimer, D. Ober, N. Maynard, W. Burke, M. Collier, D. McComas, N. Ness, and C. Smith. Variable time delays in the propagation of the interplanetary magnetic field. *Journal of Geophysical Research*, 107(A8), 2002.

C.-C. Wu and R. Lepping. Effect of solar wind velocity on magnetic cloud-associated magnetic storm intensity. *Journal of Geophysical Research*, 107(A11), 2002.

Z. Xiang, B. Ni, C. Zhou, Z. Zou, X. Gu, Z. Zhao, X. Zhang, X. Zhang, S. Zhang, X. Li, et al. Multi-satellite simultaneous observations of magnetopause and atmospheric losses of radiation belt electrons during an intense solar wind dynamic pressure pulse. In *Annales Geophysicae*, volume 34, pages 493–509. Copernicus GmbH, 2016.

G. Zhang and L. Burlaga. Magnetic clouds, geomagnetic disturbances, and cosmic ray decreases. *Journal of Geophysical Research*, 93(A4):2511–2518, 1988.

T. H. Zurbuchen and I. G. Richardson. In-situ solar wind and magnetic field signatures of interplanetary coronal mass ejections. *Coronal Mass Ejections*, pages 31–43, 2006.